UNIVERSITY OF TWENTE.

Faculty of Electrical Engineering,
Mathematics & Computer Science

Improvement of Digital Signal Processing for Multichannel TDEMI Measurements

T.H.F. Hartman

July 2018

Supervisors:
Prof. dr. ir. F.B.J. Leferink
Dr. ir. A.B.J. Kokkeler
Dr. R.A. Vogt-Ardatjew
I. Bilal, MSc
D.J.G. Moonen, MSc

Preface

This report is the merged work that T. Hartman did within the group of Telecommunication Engineering (TE) at the University of Twente. It consists of 4 papers in total, three of which are related to the subject of the Master Thesis and one is created from his internship report at Astron. Two papers have been submitted to EMC Europe (Amsterdam 2018) and have both been accepted, the internship paper will be presented orally and the other will be presented via a poster. A third paper has been submitted for GEMCCON (South Africa 2018), where the review is still pending. Lastly there is the Master Thesis paper which will be the one that will be reviewed and graded by the assessment committee.

Utilizing TDEMI Measurements using a Low Cost Digitizer to Estimate the total Dwell Time for an EMI Receiver

Tom Hartman*, Niek Moonen*, Robert Vogt-Ardatjew*, Ibrahim Bilal*, André Kokkeler*, Frank Leferink*†
*University of Twente, Enschede, Netherlands, t.h.f.hartman@student.utwente.nl
†Thales Nederland B.V., Hengelo, Netherlands

***Abstract*—By analyzing electromagnetic interference (EMI) based on its spectral components important time domain information is lost. The fact that EMI receivers, such as the Rohde & Schwarz ESS, operate this way makes them vulnerable for not detecting sources of EMI that repeat over time. The concept of EMI repeating over time is also not incorporated in the standards, which are only based on frequency domain limits. To catch these repeating interferences the receiver has to measure for at least one period of the repetition. Measuring many spectral components for a minimum amount of time each causes detrimental measurement times. Time-domain electromagnetic interference (TDEMI) analyzers have been proposed to reduce these long measurement times, but remain expensive. To reduce costs the utilization of TDEMI measurements using a low cost digitizer is examined. A PicosScope in conjunction with Digital Signal Processing (DSP) is used to create the possibility to estimate the total measurement of the ESS based on the dwell times. A short-time Fourier transform (STFFT) is used to examine the interfering source in both frequency and time simultaneously. Constrains inherent to this processing are discussed, such as the effect of windowing in the time domain. It was also shown that the ESS perceives certain time varying signals as continuous waves due to the spectral nature of this receiver. It is found that the DSP still struggles with unknown input cases. For this an adaptive threshold is proposed to detect significant low frequencies which in its simplest form improves the DSP.**

I. Introduction

Analyzing electromagnetic interference (EMI) was traditionally done based on the spectral components of the interference. This was done because a time domain analysis was still insufficiently accurate due to limitations of hardware, either due to the limited Analog to Digital Converter (ADC), sampling rate, memory or dynamic range [1]. The use of an EMI test receiver overcame these issues by analyzing each frequency bin individually while sweeping through the spectrum. This however came with certain trade-offs. Take for example how radiated emission measurements of magnetic fields are performed according to military standards (NRE01, RE101) [2] [3]. These measurements are performed between 30 Hz and 100 kHz, with bandwidths starting at 10 Hz and steps of 5 Hz. This gives rise to a lot of measurement steps that have to be taken. Also, due to the spectral analyzing nature of these receivers, time domain information is lost. This time domain information is important, because if an interference source is only apparent, for example, once every second, measuring for only half a second will not assure that the interference is measured. This fact of an interference repeating over time is also not incorporated in the standards, which are specified as a threshold over frequency [4]. To still notice the effect of the time domain variation these receivers have to measure every frequency bin for a certain amount of time, with two parallel detectors. A well founded description of analyzing time variant disturbances can be found in [5], where a simulation model is developed to mimic these types of detectors. The measurement time per frequency bin, the dwell time, is dependent on the time variation at that specific frequency. A lot of measurement steps and a minimum amount of measurement time per frequency bin result in a very long and detrimental measurement time, as has been shown in [6]. Additionally, having to do these measurements at many different positions around a large equipment under test (EUT) increases the total measurement time even more, for some systems this can even be as long as one week, resulting in very high costs. To reduce these long and therefore expensive measurement times time-domain electromagnetic interference (TDEMI) analyzers became very popular, but remain expensive. Advantages [6], [7] and challenges [8], [9] of TDEMI analyzers have been discussed previously. In this paper, a low cost digitizer known as a PicoScope is used in conjunction with Digital Signal Processing (DSP). With this DSP, it is proposed to quickly determine the minimum dwell times needed at every frequency bin. This can be used to make an estimation of the total measurement time needed for a traditional EMI receiver. The EMI receiver used in this paper is the Rohde & Schwarz ESS [10]. To accomplish the comparison, a short-time Fourier transform (STFFT) is used to create a spectrogram that holds information in both the frequency and the time domain. From this, the time repetitive behaviour of frequencies is retrieved and analyzed by taking a fast Fourier transform (FFT) of the time slice and studying the lowest significant frequency.

This paper starts with a description of the DSP and the constraints that arose. After this some time varying signals are mentioned and the way the ESS perceives time varying signals is being discussed. It is important to notice that in a general case, EMI is non deterministic and the DSP should therefore ultimately be able to handle any sort of input. For this paper, however, known input sources are proposed to get a

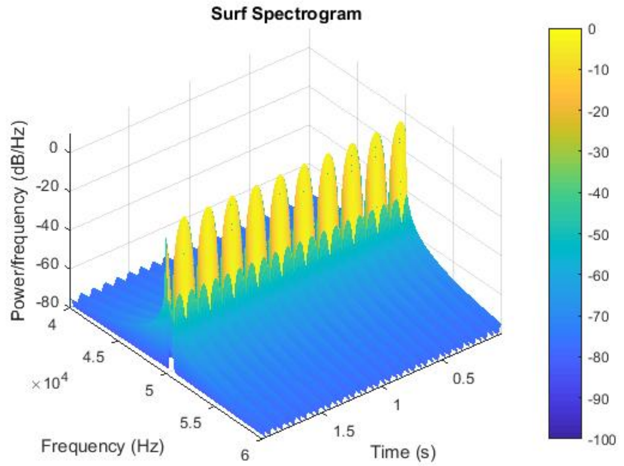

Fig. 1: Example spectrogram of a time variant signal

better understanding of the DSP and the inner workings of the traditional EMI receiver. The perception of the ESS on time varying signals is then further elaborated on in the following section where the dwell times will be analyzed. This section ends with a small discussion on an unknown input signal and ways this signal could eventually be processed correctly. This is then all wrapped up in the conclusion.

II. Digital Signal Processing

In this section, several constrains due to the spectrogram technique that is used are addressed. An example of such a spectrogram can be seen in Fig. 1, where power per frequency is shown over frequency and time simultaneously. In this figure, one can clearly see the time varying aspect of a frequency component. A spectrogram is created by taking STFFTs of the input signal where the short time is defined by a window. This window is then shifted over time while still keeping a certain overlap, to increase the time resolution. The dwell time is found by taking FFTs of the time slices at every frequency bin. From these FFTs, the lowest significant frequency is chosen which represents the inverse of the dwell time.

A. Frequency resolution of the spectrogram

The first constraint is due to the fact that the DSP is supposed to mimic the ESS. If one would be interested in the lower frequencies the standard of RE101 should be used as a guideline [2] [3]. The standard defines different bandwidths for different frequency ranges as seen in Table I. From this table, the bandwidths could be found which can then be seen as the frequency resolution of the spectrogram, also known as the step size of the frequency axis. This resolution can be seen as the inverse of the length of the window, in seconds, or as the maximum attainable frequency divided by the number of bins created. The inverse of the window length can be written as:

TABLE I: ESS parameters for a sine wave from RE101

Frequency Range	Bandwidth	Step Size	Measuring Time
30 Hz - 1kHz	10 Hz	5 Hz	2 seconds
1 kHz - 10 kHz	100 Hz	50 Hz	0.2 seconds
10 kHz - 100 kHz	1 kHz	500 Hz	0.02 seconds

$$f_{res} = \frac{1}{T_w} = \frac{1}{\frac{N_w}{fs}} = \frac{fs}{N_w} \tag{1}$$

where fs is the sampling frequency, N_w is the window size, and f_{res} could conform with the specified bandwidths defined in Table I if one is interested in these ranges.

B. Frequency resolution of the repetition rate

The second constraint, or the second effect, to take into account is the frequency resolution of the repetition rate at a certain frequency. This so called repetition rate resolution is dependent on the number of steps the time dimension of the spectrogram has. These steps in the time dimension are inversely proportional to the window length and the overlap of the windows that is chosen. This is due to the fact that the non-overlapping part of the window, also known as the window shift, can be seen as the time steps that are taken by the spectrogram. The number of window shifts and the width of such a shift have a direct influence on the actual resolution of the FFT that is performed. This is because the maximum repetition frequency is dependent on the width of the window shift and the resolution of this FFT is dependent on the number of window shifts that fit within the total time signal. This repitition rate resolution can be written down mathematically as:

$$F_{rep_{res}} = \frac{\Delta F_{\text{max}}}{N_{\text{time}}} \tag{2}$$

where ΔF_{max} is the maximum frequency difference, including negative frequencies, and equals the inverse of the time step and N_{time} is dependent on the window size and its overlap. Equation (2) can therefore be rewritten into:

$$F_{rep_{res}} = \frac{\frac{1}{\Delta T}}{floor(\frac{N_t - N_{\text{overlap}}}{N_{\text{non|overlap}}})}$$

where in the numerator, ΔT, is entirely dependent on the non overlapping part of the window, also known as the window shift, and can be written as $\Delta T = \frac{N_{\text{non—overlap}}}{fs}$. Furthermore, in the denominator, within the floor function, the number of window shifts that fit inside the whole time signal, minus one overlap is written out. If this value is not an integer number, the spectrogram function in MATLAB rounds it down to the next integer and for this reason the floor function is introduced. Within this denominator N_t is the total number of samples in the whole time signal and can be written as $T_t \cdot fs$. This all then gives rise to the following overall equation:

$$F_{rep_{res}} = \frac{\frac{fs}{N_{\text{non}|\text{overlap}}}}{floor(\frac{T_t \cdot fs - N_{\text{overlap}}}{N_{\text{non}|\text{overlap}}})} \tag{3}$$

where it can be seen that if the total measurement time is increased enough, the contribution of the window overlap on the total measurement length becomes negligible and the equation goes towards $\frac{1}{\Delta T}$. This result is as expected if we look from a definition perspective, since the lowest frequency variation over time that can be observed has a period of the total measurement time.

C. Maximum window shift

The next thing to keep in mind is the fact that the aforementioned window shift, non-overlapping part of the window, should be small enough such that the repetition over time of a frequency component is still observed. This is written down as follows:

$$a \cdot N_{\text{non}|\text{overlap}} \leq N_{rep} = T_{rep} \cdot fs = \frac{fs}{f_{rep}}$$

where a is the amount of shifts that should at least fit within one repetition rate period. Following Nyquist it is expected that a should equal 2, but from simulations it was found that this still causes some errors, due to other limitations. To prevent these errors however, it is proposed to have a be at least 4, since this can be easily satisfied with the computing power of a modern computer.

D. Windowing

As previously mentioned, to create the spectrograms, windowing is performed to create the STFFTs. These windows in the time domain also have an influence on the results in the frequency domain. The windows act as a multiplication in the time domain which results in a convolution in the frequency domain. For theoretical simplicity a rectangular window is chosen in this section. This rectangular window then results in a sinc function around the corresponding frequency components in the frequency domain. This sinc function will then have an influence on other frequency components where there is no zero crossing. It is important to notice however, that the spectrogram has discrete steps in the frequency domain which are dependent on the window size. If the window size is chosen as an integer multiple of the frequency difference between frequency components, the resulting sinc function has zero crossings at all the multiples of the frequency resolution around its frequency component, and the effect of windowing will not be present in the simulation. This is written down mathematically as:

$$f_{\text{zero}} = f_c \pm \frac{n \cdot fs}{N_w}$$

where f_{zero} are the zero crossings of the sinc function, f_c is a frequency component, n is any positive integer, and where the width of the sinc function is dependent on the window size. Because of these zero crossings at the other frequencies, no variation at the individual frequency components will be noticed, even in simulation. If this is not the case however, the sinc function at one frequency component does have an influence on others and vice versa. This then means that a time variation becomes apparent at the frequency components and will be noticed. This case is visualized in Fig. 2. The window size is not a integer multiple of the frequency difference between frequency components and it can be seen that at the other frequency components the sinc function does not have a zero crossing. It is important to note however that in this case the sampling is not exactly at the desired frequencies. If the sampling is exactly at the desired frequencies however, it has been shown that the sinc function always has a zero crossing on the other sampled frequencies. This is because the relation of the frequency resolution, which has an influence on the sampling steps, and the relation of the width of the sinc function, are both dependent on the windowing. In a real case, with an unknown input signal however, there will always be frequency components at different spots than the sampling moments. This then means that frequency components will influence each other even when this would not be the case for the ESS, which is a detrimental effect when mimicking the ESS. An example of this effect will be discussed in the measurement results.

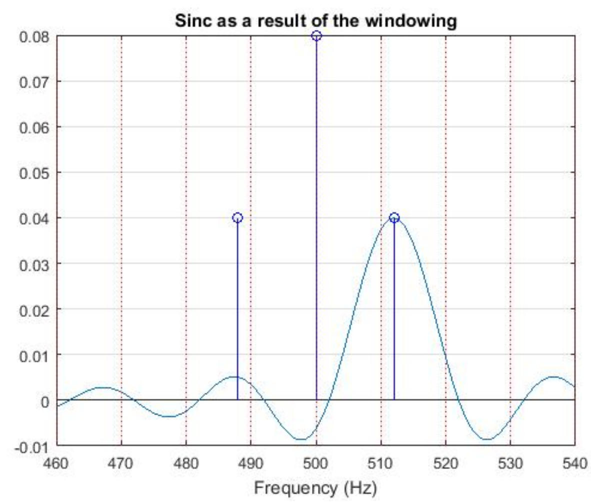

Fig. 2: Example of the windowing causing errors

III. Time Varying Signals

In this section some examples of time varying signals are presented to inspect the time varying nature of EMI. This is followed up by an explanation of how the ESS filters the input signals and the influence it has on the perception of these time varying signals.

A. Signals

The signals used for measurements are created with a signal generator and measured with the ESS parallel to the PicoScope. The time-domain data measured with the PicoScope is then processed by the algorithm to check if the

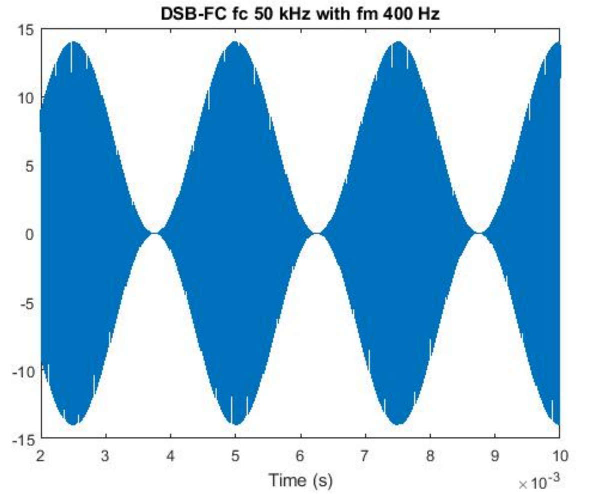

Fig. 3: DSB-FC at 50 kHz with 400 Hz variation

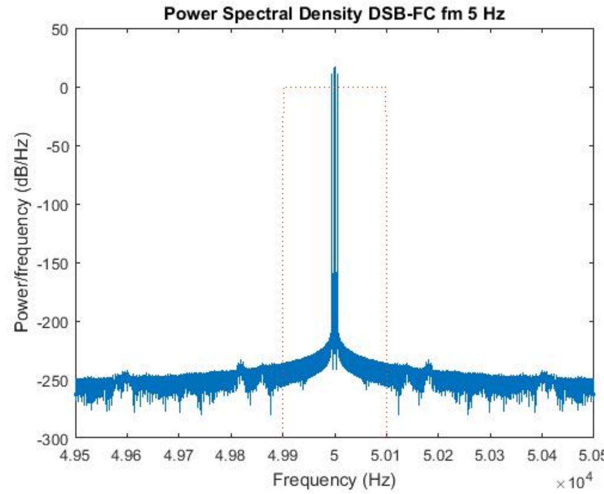

Fig. 4: DSB-FC with all frequency components in one filter bank

same dwell times are found as the results given by the ESS. Several types of signals could be used with a time variant behaviour of their frequency components. One can think of, (random) On-Off keying, a chirp signal, Frequency Hopping of Bluetooth, a double-sideband surpressed-carrier (DSB-SC) and a double-sideband full-carrier (DSB-FC). In this paper a DSB-FC signal is used for the main analysis and an example of such a signal can be seen in Fig. 3. This signal is used because of its time varying nature and because it is easily produced via a signal generator. While testing this signal some constraints arose about the definition of a time varying frequency component which will be further elaborated on. Apart from this an unknown input source is also used to further discuss the performance of the DSP.

B. Filter Bank

As previously mentioned, the ESS analyzes EMI by its spectral components. It does so by going through all the frequencies within a range step by step. This can be seen as a filter bank shifting over the entire frequency range with a certain step size. Analyzing the frequency components in their individual filter banks separately raises some questions. Looking from the time domain perspective Fig. 3 clearly resembles a signal with a high frequency component varying over time. Put even more strongly, the whole definition of this test case was to create a high frequency component which varies over time with a lower frequency component. This input signal is written down mathematically as:

$$A(t) \cdot cos(2\pi f_h t),$$

where $A(t) = 1 + cos(2\pi f_l t)$, f_h is the high frequency and f_l is the low frequency. We know however that this can be seen as two individual frequency components around a high frequency component because:

$$cos(\alpha) \cdot cos(\beta) = \frac{1}{2} \cdot [cos(\alpha - \beta) + cos(\alpha + \beta)]$$

From this point on, the frequency resolution seen in equation (1), which can be seen as the width of a frequency bin of a filter bank, has a huge impact on how the signal is perceived. This is due to the fact that if this frequency bin width becomes smaller than the difference between adjacent frequency components it will not catch both frequency components simultaneously. This is visualized in Fig. 4 and Fig. 5, where the frequency components are received in one frequency bin and in separate frequency bins respectively. The frequency bins are chosen to have a width of 200 Hz, because this is the minimum width of the quasi-peak detector used in the ESS. The use of this quasi-peak detector will be further elaborated on later. If the frequency components are received in separate bins for the EMI receiver it is expected that it will perceive the signal as individual frequency components which are not varying over time, also known as individual continuous waves at different frequencies. This case with the EMI receiver will further be elaborated on in the results.

IV. Dwell Time Analysis

In this section the results will be presented. At first the ESS measurements of the two DSB-FC cases are compared. From these results it is shown that one signal is perceived as time varying while the other is not. The signal perceived as time varying is then further inspected and the time variation is presented after which this result is then mimicked with simulations. After this an unknown input source is used and the performance of the DSP is discussed.

A. DSB-FC comparison

For these measurements two signals such as shown in Fig. 3 are used. The first measurement uses a high frequency component of 50 kHz which is smoothly turned on and off with a 5 Hz sinusoid, the second signal is the one shown in Fig. 3 and has the same high frequency component of 50 kHz but is smoothly turned on and off with a 400 Hz sinusoid.

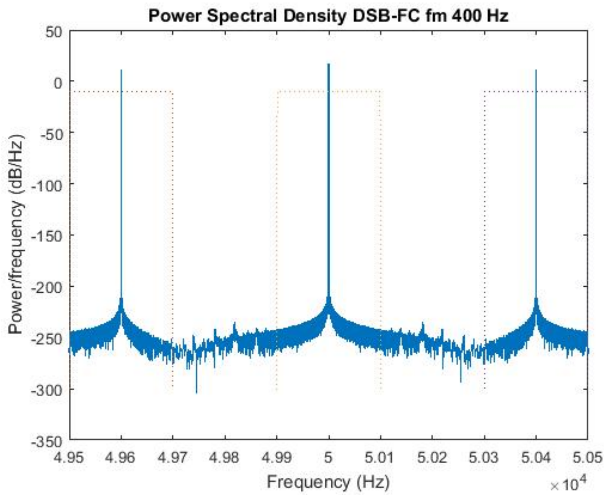

Fig. 5: DSB-FC with one frequency component per filter bank

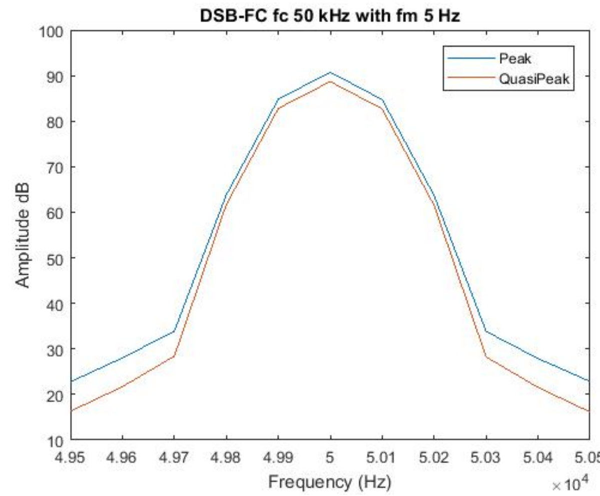

Fig. 6: Peak vs Quasi-Peak detector of DSB-FC (5 Hz)

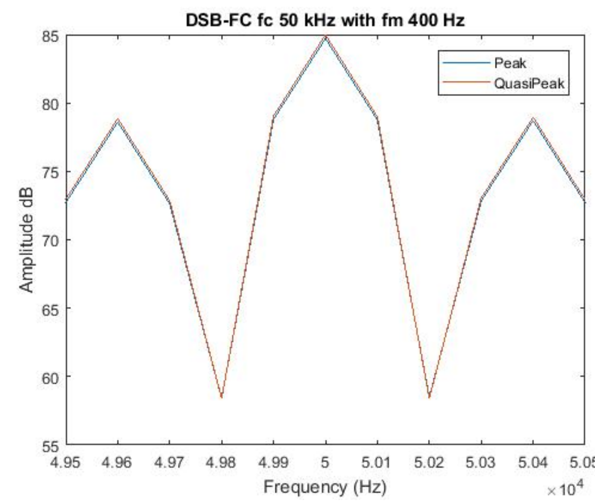

Fig. 7: Peak vs Quasi-Peak detector of DSB-FC (400 Hz)

1) DSB-FC comparison with ESS: The first measurement performed is measuring the signal simultaneously with two detectors over a certain frequency range. The two detectors used are peak and quasi-peak detectors. This is done to show whether or not the frequency components are continuous waves. This is done because we know that a frequency component is a continuous wave if the peak and quasi-peak detectors give the same output [11].

In Figures 6 and 7 these results are shown. In Fig. 6 a clear difference between peak and quasi-peak can be seen meaning the signal is not a continuous wave, which was as expected when looking at the time signal. Fig. 7 shows three frequency components not varying over time, since there is almost no difference between peak and quasi-peak. Upon further examining Fig. 7 a difference of 0.2 dB is found between peak and quasi-peak. This variation is small enough to consider the signal as a continuous wave. It is important to note however that the quasi-peak detector was 0.2 dB higher than the peak detector and not the other way around, which would be as expected. Under normal circumstances the quasi-peak detector should always give an output lower or equal to the output of the peak detector. As a check a known individual continuous wave was put on the ESS, and the same detectors were used simultaneously. For this measurement the same deviation of 0.2 dB was found between the peak and quasi-peak detectors and it can therefore be seen as a measurement error inherent to the ESS.

2) Inspecting the dwell time: Next up the dwell time will be measured via the ESS and calculated via DSP. From Fig. 7 it was shown that this case was perceived as three individual continuous frequency components and will therefore not be further investigated with the ESS, because no dwell time will be found. The signal is however investigated via DSP. For this case it is important to note that the frequency components appear exactly at the sampling moments. This makes it so that the influence of the windowing in this case is non existing. Because of this, no time variation at the frequency components will appear and the right result of no repetition over time will be given. If the slow varying frequency was changed to, for example, 401 Hz, however, the effect of windowing at all the frequency components would have an influence on all the other ones, just as seen in the example from Fig. 2. This would then result in a noticeable time variation which will be spotted and therefore give different results than the ESS. This effect should be further investigated later on, but for now it is seen as future work. Using different window types has an impact on this influence and is part of this future work.

Next up the dwell time, shown in Fig. 6 to exist, was measured via the ESS and calculated via DSP. The dwell time is found via the ESS by measuring the peak n times for different measurement times. For these measurements n is chosen as 30. This is then plotted versus each other from which we can see the peak distribution convert to one specific value at a certain measurement time. This can be seen in Fig. 8 where all the peak measurements give the same output with a

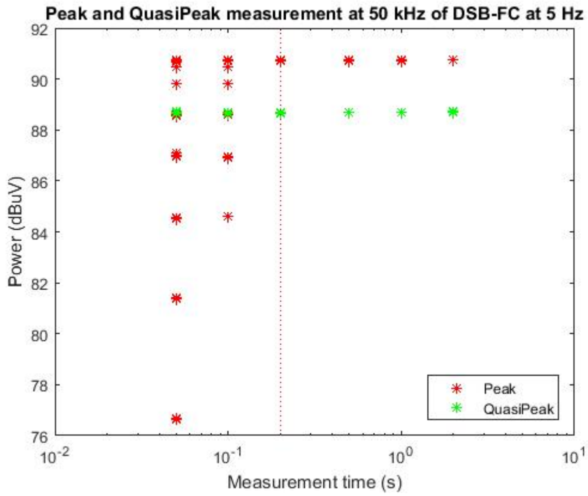

Fig. 8: Finding Dwell Time of DSB-FC (5 Hz) with the ESS

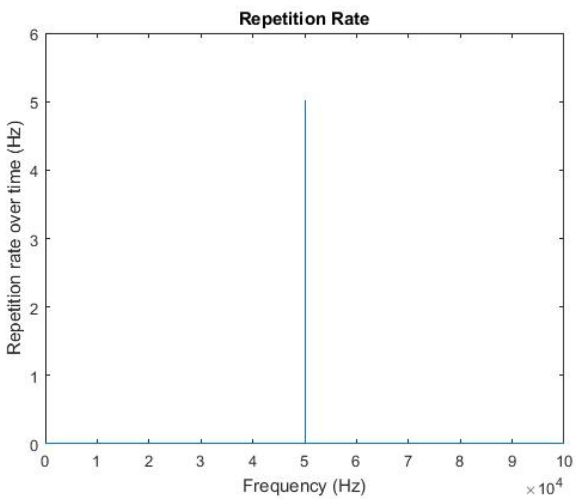

Fig. 9: Finding Dwell Time of DSB-FC (5 Hz) with DSP

measurement time of 0.2 seconds, which implies a repetition frequency of 5 Hz. The same is found via DSP from which the same repetition rate is quickly calculated, for all frequencies, and can be seen in Fig. 9.

B. Unknown Input Signal

Doing the basics of the DSP for any input signal does not give rise to any direct problems. Taking a STFFT is easily achieved by a computer nowadays. Once the resulting spectrogram has been created, taking the FFT of every time slice of a certain frequency can also be achieved with relative ease, if the aforementioned constrains are taken into account. From this point on a problem arises however. When no information is known about the input source whatsoever, the program should be able to snuff out the lowest significant frequency, where defining this significance raises issues. One proposed technique to detect these significant frequencies is creating a threshold where the first peak above this threshold is considered as the frequency repetition. Such a threshold should lie between zero and the maximum peak of the FFT at a frequency component. Where if a threshold of zero is applied, the first frequency component would always be selected, which results in a dwell time equal to the total measurement time, with a small deviation due to equation (3). Defining the height of this threshold could be based on empirical results for certain cases. It is also proposed to take the peak to average power into account. This in combination with a well justified definition of a significant low frequency could give rise to an adaptive threshold for any input signal. These proposals are however, outside the scope of this paper and will be investigated later except for the influence of the threshold which will be examined below.

1) Dwell Time: To elaborate on the influence of such a threshold a random signal has been processed. The resulting spectrogram of the signal can be seen in Fig. 10. First the dwell times were found by taking the maximum peak of the FFT of a time slice of every frequency bin. If only the maximum peak of the FFT of every time slice is chosen, there is a chance, that still significant, low frequency repetitions are neglected because a higher frequency repetition has more power. An example of such a case is shown in Fig. 11. One can clearly see that there is a significant lower frequency component at 33 Hz, but this one is not selected if only the maximum peak technique is used. This results in dwell times that are too short, because there are still significant low frequencies, which need longer dwell times to be detected, that are missed. This can be seen in Fig. 12 where short dwell times are shown around 30 kHz, while if we look at the spectrogram we also see a slower repetition rate, which means a longer dwell time of roughly 0.03 seconds, which is still significant. This occurs because of the problem previously mentioned and shown in Fig. 11. This figure shows the FFT of the time slice at 30 kHz. To be able to detect this significant lower frequency a threshold of 90% of the maximum peak at every FFT is applied. It is important to note that this is still a crude solution and should be improved later on, as previously mentioned, but already has a huge improvement on the results. The result of this adaptive threshold is seen in Fig. 13. With this threshold the significant lower frequency repetitions are detected for the frequencies around 30 kHz. This result therefore proposes longer measurement times compared to the maximum peak technique, but decreases the error significantly. The error difference is quantified by comparing the maximum peak of the total time signal at a frequency component with the average of the peaks found for multiple measurements at random points in the time signal for the found dwell time. The maximum peak technique detects peaks 4.7 dB lower than the maximum peak on average while the technique using a threshold of 90% detects peaks 1.9 dB lower than the maximum peak on average. From the end result of the DSP the dwell times could be added up for every frequency bin which then gives an estimation of the time the ESS would have to take to detect all the, repeating, interferences, depending on the dwell times and the frequency bin size.

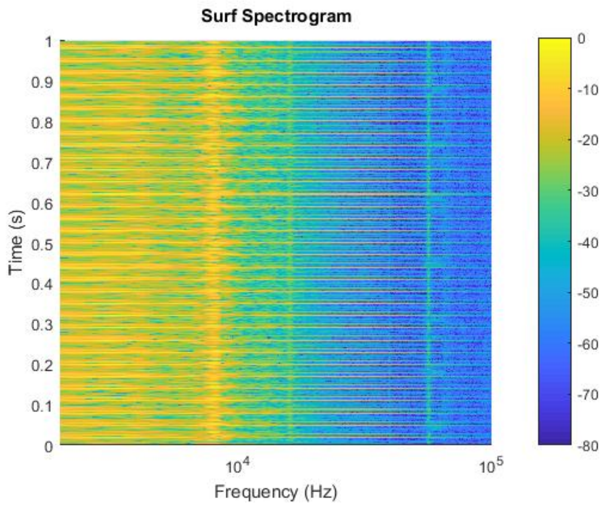

Fig. 10: Spectrogram of Conducted Measurement

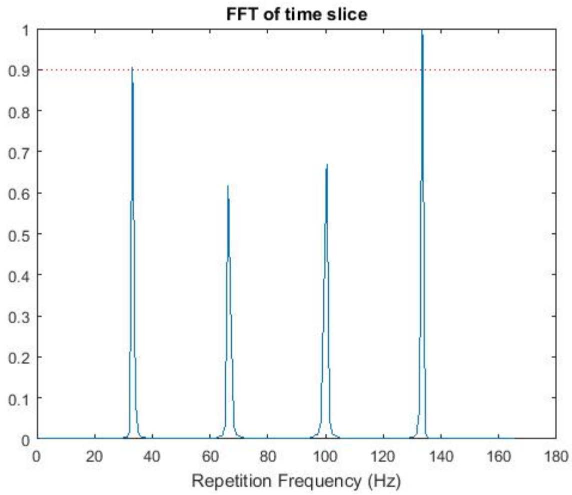

Fig. 11: Normalized FFT of a time slice at 30 kHz

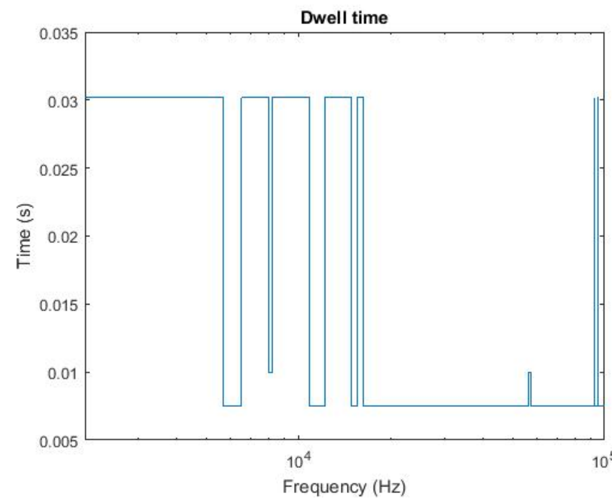

Fig. 12: Dwell Time using Max Peak

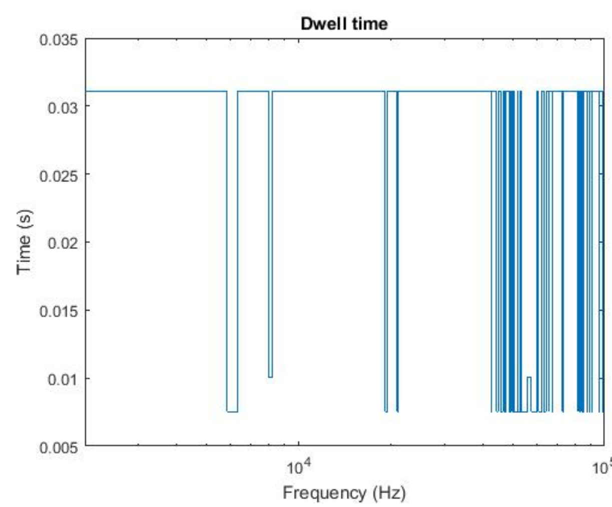

Fig. 13: Dwell Time using a Threshold of 90%

V. Conclusion

Utilizing TDEMI measurements with a low cost digitzer via DSP to estimate the dwell times for an EMI receiver has been investigated. Several constrains have been mentioned on the DSP part which should be taken into account when further investigating this topic. These consisted of the frequency resolution of the spectrogram which can be seen as the width of a filter bank, the resolution of the repetition rate which goes towards one over the measurement time, and the effect of the window and its shift. Several time varying signals are mentioned and the way the ESS perceives these signals is elaborated on. This perception of the ESS is then further investigated together with the effect it has on mimicking the ESS via DSP. This is explored by doing a dwell time analysis on two types of DSB-FC signals, which have the same carrier frequency but a different amplitude variation. This dwell time analysis was performed by using a peak and quasi-peak detector simultaneously to examine whether the input is a continuous wave or not. It was shown that for one case the ESS perceives the DSB-FC as time varying while in the other it perceives it as continuous waves at different frequencies. This is fully dependent on the frequency bin size of the detectors in the ESS, in this case predominately the quasi-peak detector, and the amplitude variation of the signal itself. The time varying signal is then measured with the peak detector multiple times, for different measurement times, to create a distribution of peak values. This distribution then converges to one value at the sought dwell time. This paper then opens a road for further research on the DSP, especially considering unknown input signals, the influence of windowing on such signals and the effect of different window types on any signal whatsoever.

References

[1] E. Puri and M. Monti, "Pitfalls in Measuring Discontinuous Disturbances with Latest Click Analysers," *Emc2016*, pp. 1–6, 2016.

[2] S. M. A. Solar and T. Ag, "Electromagnetic (Environmental) Compatibility," no. January, pp. 1–8, 2011.

[3] MIL-STD, “Requirements for the Control of Electromagnetic Interference Characteristics of Subsystems and Equipment,” *Measurement*, no. March, pp. MIL–STD, 2015.
[4] I. Setiawan, C. Keyer, F. Buesink, and F. Leferink, “Time-frequency diversity for solving e deadlock in defining interference levels in power lines,” *IEEE International Symposium on Electromagnetic Compatibility*, vol. 2016-Novem, pp. 364–369, 2016.
[5] T. Karaca, B. Deutschmann, and G. Winkler, “EMI-receiver simulation model with quasi-peak detector,” *IEEE International Symposium on Electromagnetic Compatibility*, vol. 2015-Septm, pp. 891–896, 2015.
[6] I. Setiawan, N. Moonen, F. Buesink, and F. Leferink, “Efficient Magnetic Field Measurements,” 2017.
[7] M. Pous, M. Azpúrua, and F. Silva, “Benefits of Full Time-Domain EMI Measurements for Large Fixed Installation,” pp. 514–519, 2016.
[8] E. Puri and M. Monti, “Hidden Aspects in CISPR 16-1-1 Full Compliant Fast Fourier Transform EMI Receivers,” pp. 34–39, 2016.
[9] ——, “The Importance of Overload Revealing in EMI Receivers,” 2017.
[10] Rohde & Schwarz, “Operating Manual EMI Test Receiver ESS 1011.4509.30.pdf,” Tech. Rep.
[11] Keysight, “Keysight X-Series Signal Analyzers, Measurement Guide,” p. 83.

Direct Sampling in Multi-channel Synchronous TDEMI Measurements

Tom Hartman*, Niek Moonen*, Frank Leferink*†
*University of Twente, Enschede, Netherlands, t.h.f.hartman@student.utwente.nl
†Thales Nederland B.V., Hengelo, Netherlands

***Abstract*—This paper shows possible benefits of multi-channel synchronous time-domain electromagnetic interference (TDEMI) measurements. The setup was developed with respect to low-frequency conducted Electromagnetic Interference (EMI) measurements in high power, fast switching systems using a low-cost solution. Using an 8-channel digitizer voltages, currents and magnetic fields were simultaneously recorded. Using digital signal post-processing investigations are performed into the relation between switching currents and magnetic fields, while also investigating the time variance of the load impedance.**

I. Introduction

EMI has been traditionally analyzed based on their spectral content. Due to the limitations of hardware, time domain analysis was insufficiently accurate. Either due to the limited Analog to Digital Converter (ADC), sampling rate, memory, or dynamic range [1]. Using an EMI test receiver, overcame these issues by analyzing each frequency bin/band individually while sweeping through the spectrum. Inherently, the switch to super-heterodyne receiver introduced trade-offs. Measurement times increased, while time domain information was lost in the peak detector, therefore correctly analyzing the disturbance requires the disturbance to be repetitive in nature, while maintaining a constant amplitude. Different types of detectors addressed this issue. A good explanation of analyzing time variant disturbances can be found in [2], since a simulation model is developed to mimic different types of detectors. To summarize, issues with super-heterodyne receivers are often related to the type of the disturbance being unknown.

- narrowband vs broadband
- continues wave vs transient
- time-consuming

With the recent development of fast Fourier transform (FFT) based Receivers, EMI measurements have become much easier. Several TDEMI measurement techniques have been studied [3]–[5]. Digital decomposition of Common Mode (CM) and Differential Mode (DM) has been shown in for instance [3], [6], this requires a multi-channel approach. Transient decomposition is shown in [7] using short term fast Fourier transform (STFFT) techniques. While in [4], [8] it is proposed to use STFFT techniques to present time-frequency plots (i.e. spectrograms), however engineers need to be trained in analyzing these results, and standards still need to be developed. However the biggest drawback, is that the Commercial of the Shelf (COTS) available FFT-receivers are single input with a heterodyne chain.

With the development of low-cost digitizers, the possibility for creating ones own low-cost receiver arises. It has for instance been used in developing a cost effective and fast magnetic emission test platform [9].

This paper will focus on applications of multi-channel synchronous measurements as stated in [5] and the possible challenges it brings. In [6] it was applied to decompose, and compare multiple measurement techniques. This paper will show the possibility to investigate magnetic emissions related to switching transients, and also the possibility to analyze a time variant impedance. In either case, a synchronous multi-channel solution is required. An 8-channel digitizer has been used to record the phase-, neutral- and DM- current and voltages. Additionally the magnetic field has also been recorded according to the RE101 standard.

The general overview of the total measurement can be found in [6], which focuses on the conducted part of the measurement. The 8-channel scope is used in conjunction with the 'mains monitor box' as described in [10] and will be elaborated on in Section III. Voltage and current measurements have an overlapping bandwidth from approximately 2 kHz to 100 kHz. Next to conducted measurements, the radiating magnetic field is recorded to investigate its relation to fast switching currents. The results presented in section IV are qualitatively reviewed, as this is a proof-of-concept type of setup.

II. Theoretical Background

The multi-channel approach allows for exploration in the unknown and novel domains at relative low costs. As was explained, in this paper we aim for the current to magnetic relationship, and the concept of a time varying impedance. In the following subsections, the concepts are further explored and the motivation for exploration is given.

A. Magnetic Field

As is well known from the Maxwell equations, a current induces a magnetic field and furthermore magnetic fields induce currents as is explained by Lenz's law. We measure magnetic fields with loop antennas, which act as transducers for magnetic flux. I.e. an output voltage of the antenna is

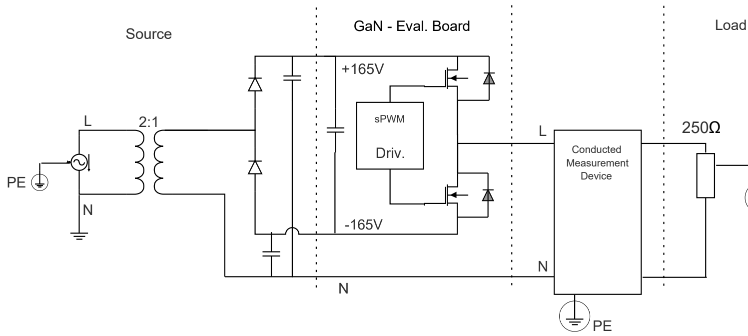

(a) setup

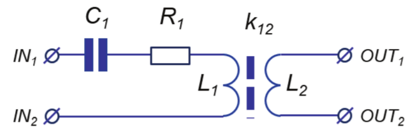

(b) Filter insulator implementation adopted from [10]

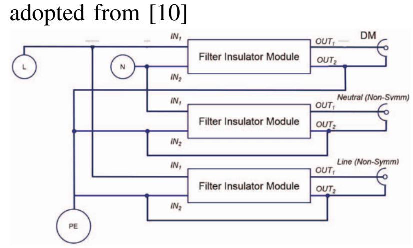

(c) A single phase implementation adopted from [10]

Fig. 1: Schematic representation of the test setup [6]

created by means of a varying magnetic flux, which can be seen using the following equations:

$$\mathcal{E} = -\frac{d\Phi}{dt}, \qquad \Phi = \iint_S \mathbf{B} \cdot dA$$

$$\oint \mathbf{B} \cdot d\mathbf{l} = \mu_0 I_{enc}$$

From these we can see a proportional relationship exists between the time-derivative of the current inside a system and the measured magnetic field:

$$\mathbf{B} \propto \frac{di}{dt}$$

In the measurement setup, current and magnetic field have both been recorded simultaneously. This allows for an investigation into the radiation transfer function (radiation efficiency) of the entire system. The relation between E-field and varying voltage has been researched in [11]. Following the same assumption of a Linear Time-Invariant (LTI) system shown in this paper, a possible attenuation profile might be derived. However the amount of measurements in this setup are limited and since the focus of the paper is on the multi-channel low cost digitizer possibilities, a full study of transfer function of the system is regarded to be future work.

The digital signal processing done for this work, is related to the MIL-STD RE101. We want to examine the relation between transients and B-fields in time, however the recorded signal is always a time varying voltage. The recorded signal x(t), should first be transformed into a spectrum in dBuV, to which the antenna factor can be applied. From this the time variant magnetic field can be recovered via the inverse Fourier transform.

$$\mathcal{F}[x(t)] = X(\omega), \qquad Y(\omega) = X(\omega) \cdot AF(\omega)$$

$$\mathcal{F}^{-1}[(Y(\omega))] = y(t)$$

With x(t) being the recorded voltage from the loop antenna, y(t) the magnetic field measured, and AF the antenna factor. Performing these operations will result in a complex valued time series, of which only the real values have meaning and its unit will be in pT . The imaginary part is a result of rounding errors and applying a perfect filter for frequencies above 100kHz. Assuming a perfect symmetrical spectrum around the Nyquist frequency removes this issue. In the following subsection the concept of measuring a varying impedance is addressed.

B. Varying Impedance

The varying impedance concept originates from power grid measurements, in which many users are independently inserting and extracting loads. In case of old fashioned resistive loads, this already introduced fluctuations in the power grid.

The transition to Switch Mode Power Supply (SMPS) has introduced a more difficult task in defining a load. This can already be seen in Fig. 1, as a load of $250\,\Omega$ is being used with either a positive or negative voltage. From the grid side, a constant varying $50\,\text{Hz}$ sinewave is provided. However, the current is drawn from the grid is either positive or negative depending on the switching state. A third state is also available, in case both of the switches can be considered to be open. This is during the time a deadtime is introduced, it is inserted to prevent the half-bridge from shorting.

Evaluating the varying impedance requires processing of the recorded voltages and currents. In the measurement setup as shown in Fig. 1 the voltage is recorded with a 1:10 voltage probe, while the currents are detected via a currentclamp (Pico TA189). In [6] the overlapping frequency ranges were shown, in which the measurement methods are valid. In this case we assume $v(t)$ and $i(t)$ are recorded, which are also frequency dependent. Using the STFFT in both cases, the overlapping frequencies can be extracted while maintaining the time-varying information. In that case the following relation would hold:

$$Z(f,t) = \frac{v(f,t)}{i(f,t)}$$

Note however the setup as it is shown here, will mainly address issues that arise from post-processing, as one expects to record voltages and currents running through the $250\,\Omega$ load. The resulting impedance will not be the total SMPS impedance. This was done as a verification of the post-processing.

III. Measurement Setup

Safely measuring DM EMI in a relatively high voltage (i.e. above 100 V) setup is done as depicted in Fig. 1a. The inside of a conducted measurement device, as seen in Fig. 1a, can be seen in Fig. 1b and Fig. 1c. As the emphasis of this paper lies in synchronous time domain measurements, the functional behavior of the AC/DC converter will only be briefly described here. The used quantities are magnetic field, DM voltage and DM current at the load.

A. Galium-Nitride (GaN) Half-bridge

In Fig. 1a it can be seen that the 'DC' source is a galvanic isolated grid that has been rectified. By using Sinusoidal Pulse Width Modulation (sPWM) driver logic, the switches are operated in such a way, that the switching node is either connected to the +165 V or -165 V. This results in a sPWM voltage waveform that contains two main frequency components, f_c and f_m, which are the switching frequency and AC output frequency respectively. [11] describes the full background for studying a DC/AC converter with extreme flexibility in choosing these frequencies. However, in the evaluated setup $f_c = 25\,\text{kHz}$ and $f_m = 50\,\text{Hz}$, which implies that, when the output waveform is low pass filtered, the resulting AC signal consists only of a 50 Hz component with an approximate $V_{rms} = 116\,\text{V}$.

B. Magnetic Field Measurement

The magnetic field measurement RE101 as was shown in [9] has also been performed to the above described setup, however the time domain signal was simultaneously recorded and now available for evaluation in the results section.

C. Varying Impedance Measurement

This subsection is to emphasize that the extraction of the voltage and current was done according to the previous written paper [6] and is now applied to a more elaborate processing scheme that shows the benefits of using a synchronous multi-channel digitizer.

Now that the measurement setup and processing of the results have been described, the results are presented in the next section.

IV. Results

The results will also be presented into two sub-sections following the structure applied throughout this paper. First the magnetic field results are shown, as this is a more predictable result. The varying impedance is a novel concept and is presented here as a possibility to investigate with a multi-channel digitizer. The results shown here are only evaluated qualitatively, and quantifying the results is left to future work.

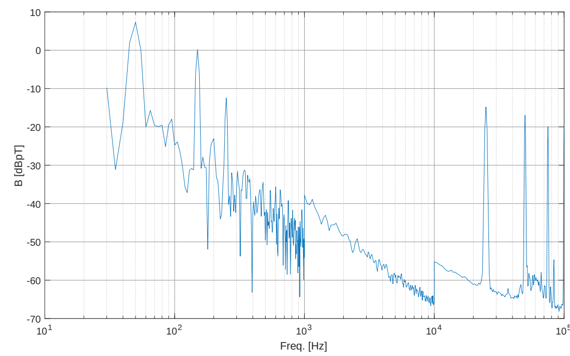

Fig. 2: Results from processing the single channel according to the RE101 standard, which is explained in [9]

A. Magnetic Field results

The measurement results are shown for the time varying magnetic field that was recorded using the standard loop antenna as is used in the MIL-STD RE101 emissions test. First the results are processed according to standard as was described in [9] and shown in Fig. 2. Emission spikes can be seen at 50 Hz, 150 Hz and 250 Hz in the lower frequency range. While in the high frequency range (above 10 kHz), the switching frequency of 25kHz and its harmonics can be seen. This validates the setup, working properly as intended. Now to examine the switching transients effects on the radiated emissions, Fig. 3 is created according to the procedure that was described in section II-A. The resulting waveform shown in red, shows during the current switching spikes that are either positive or negative depending on the transition state. The magnetic field is also slowly varying, which can be seen in Fig 4. In our measurement setup, the slowly varying component of the magnetic field is more significant that the magnetic field that is due to the fast switching of the GaN half-bridge. However, due to the applied processing both phenomena can be seen and evaluated if needed.

B. Varying Impedance Results

The results displayed in Fig.5 show amplitude spectral densities that are varying in frequency as well as time. As the impedance is calculated as a ratio of voltage and currents, a very low current can result in a very high impedance. By creating a sPWM waveform, that contains the 50 Hz as the output, while switching at 25 kHz only these frequency and their harmonics are measurable. At other frequencies the noise floor is being measured. This effect can be nicely seen in

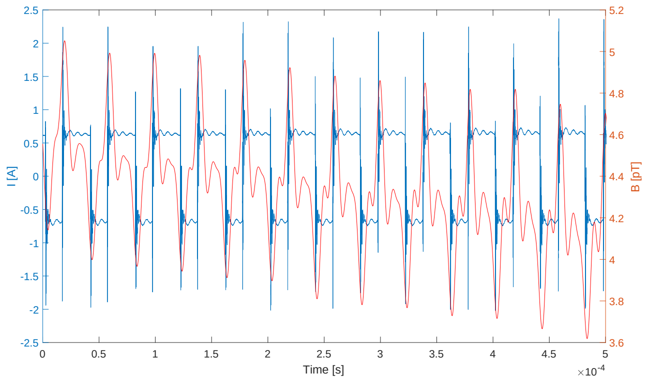

Fig. 3: The measured DM-current (blue) and magnetic field (red). The magnetic field is retrieved from

upper graph in Fig. 5 and also in Fig. 6. In Fig. 6a the current is varying between 0.06 A and 0.09 A, while in Fig. 6b the current fluctuates between approx. 0 A and 0.045 A. The resulting impedance is spiking at the moments that the current is approaches zero. From this we can conclude that the four noise bandwidths are due to the measured noise that are shown as dark blue regions, in the bottom two figures of Fig. 5.

V. Conclusion

Using an 8 channel measurement setup, multi-channel synchronous time domain measurements have been explored. Focusing on magnetic-field radiation arising from switching currents, and time variant impedances. It has also been shown that by combining low-frequency current measurements (DC-100 kHz) with high-frequency voltage measurements (2 kHz-7 MHz), one is able to evaluate the impedance in the overlapping frequency range. Issues in calculating the impedance arise from measuring low currents, that are (in this case) due the noise in the measurement system.

As the magnetic field measurement has been performed according to RE101, the entire lower frequency range was covered (30 Hz-100 kHz). Simultaneously the DM current was recorded in a frequency range of DC-100 kHz. After correction for the loop-antenna used, it was possible to see the influence of the fast switching current on the measured magnetic field. Even though the impact was lower than the slow varying component it has been shown that it is possible to benefit from multi-channel synchronous conducted TDEMI measurements applied in high power electronic systems.

References

[1] E. Puri and M. Monti, “Pitfalls in Measuring Discontinuous Disturbances with Latest Click Analysers,” *Emc2016*, pp. 1–6, 2016.

[2] T. Karaca, B. Deutschmann, and G. Winkler, “EMI-receiver simulation model with quasi-peak detector,” *IEEE International Symposium on Electromagnetic Compatibility*, vol. 2015-Septm, pp. 891–896, 2015.

[3] Y.-s. Lee, “Time Domain Measurement System for Conducted EMI and CM/DM Noise Signal Separation,” *2005 International Conference on Power Electronics and Drives Systems*, vol. 2, pp. 1640–1645, 2005. [Online]. Available: http://ieeexplore.ieee.org/lpdocs/epic03/wrapper.htm?arnumber=1619951

[4] B. J. A. M. Van Leersum, R. B. Timens, F. J. K. Buesink, and F. B. J. Leferink, “Time domain methods for the analysis of conducted interference on the power supply network of complex installations,” *IEEE International Symposium on Electromagnetic Compatibility*, pp. 605–610, 2014.

[5] M. Pous, M. Azpúrua, and F. Silva, “Benefits of Full Time-Domain EMI Measurements for Large Fixed Installation,” pp. 514–519, 2016.

[6] T. Hartman, N. Moonen, and F. Leferink, “Evaluation of Multichannel Synchronous Conducted TDEMI Measurements for High Voltage Power Electronics,” in *2018 International Symposium on Electromagnetic Compatibility - EMC EUROPE*, 2018, p. to be published.

[7] M. A. Azpúrua, M. Pous, and F. Silva, “Decomposition of Electromagnetic Interferences in the Time-Domain,” *IEEE Transactions on Electromagnetic Compatibility*, vol. 58, no. 2, pp. 385–392, 2016.

[8] I. Setiawan, C. Keyer, M. Azpurua, F. Silva, and F. Leferink, “Time-domain Measurement Technique to Analyze Cyclic Short-Time Interference in Power Supply Networks,” pp. 279–282, 2016.

[9] I. Setiawan, N. Moonen, F. Buesink, and F. Leferink, “Efficient Magnetic Field Measurements,” 2017.

[10] C. Keyer, F. Buesink, and F. Leferink, “Mains Power Synchronous Conducted Noise Measurement in the 2 to 150 kHz band,” pp. 865–869, 2016.

[11] C. V. Diemen, N. Moonen, and F. Leferink, “Estimation of Radiation Efficiency of GaN Half-bridge Based Submodule System for Radiated EMI Prediction,” in *2018 International Symposium on Electromagnetic Compatibility - EMC EUROPE*, 2018, p. to be published.

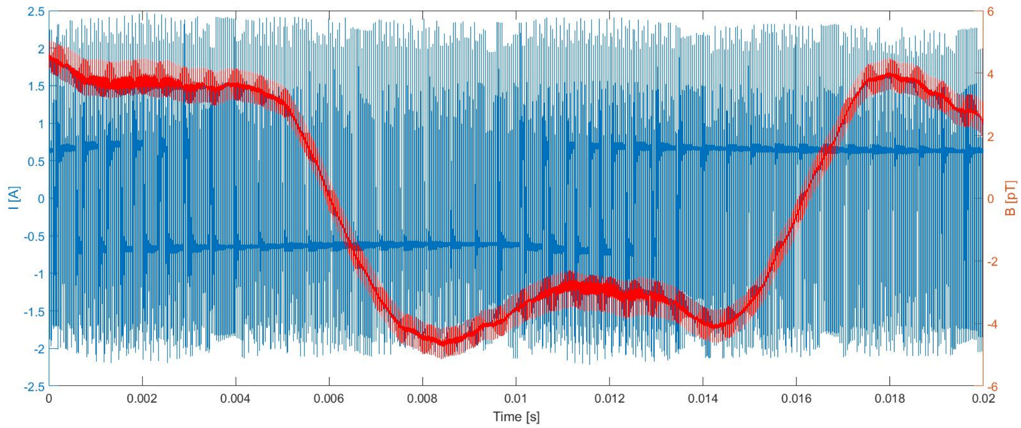

Fig. 4: The measured time signal DM-current (blue) and magnetic field (red)

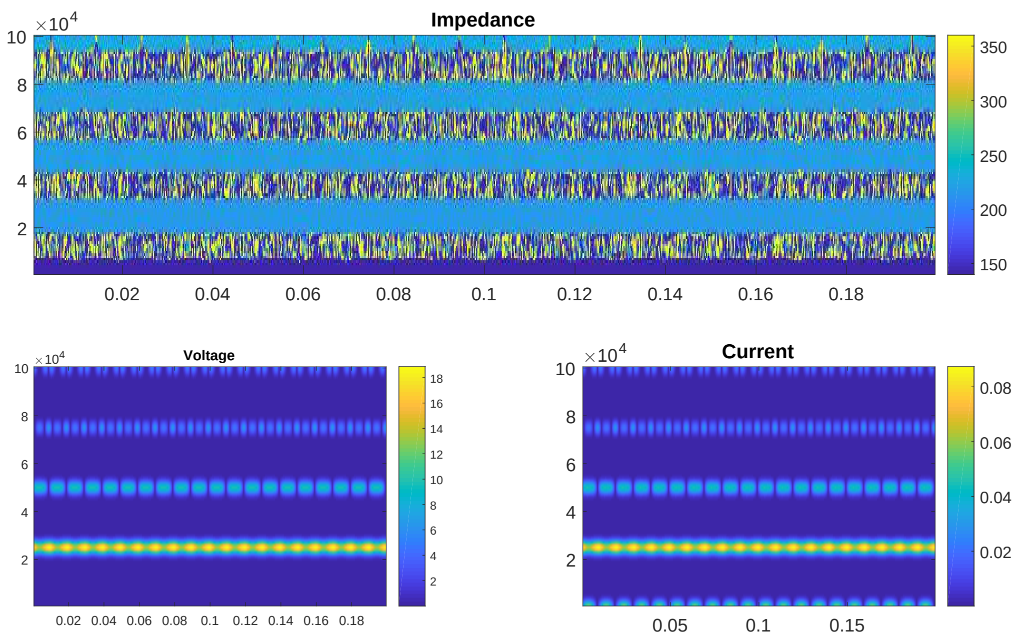

Fig. 5: The top figure displays the calculated impedance which is the ratio between the voltage STFFT and current STFFT. These are shown in the bottom figures.

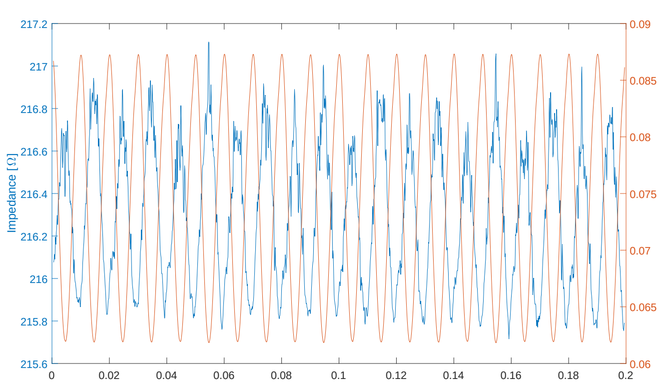

(a) Extracted impedance vs extracted current at 25 kHz

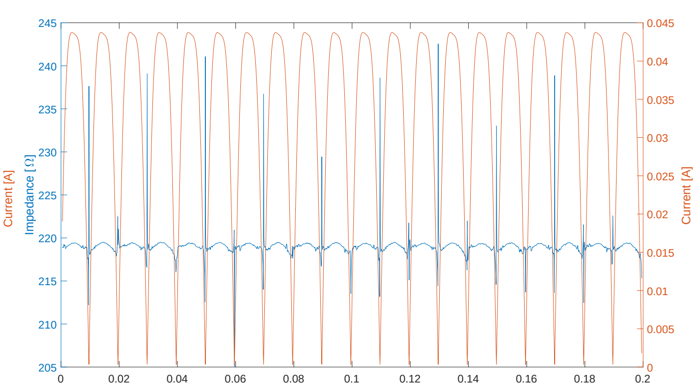

(b) Extracted impedance vs extracted current at 50 kHz

Fig. 6: The waveforms are single frequencies selected from the spectrogram displayed in Fig. 5

Evaluation of Multichannel Synchronous Conducted TDEMI Measurements for High Voltage Power Electronics

Tom Hartman*, Niek Moonen*, Frank Leferink*†
*University of Twente, Enschede, Netherlands, t.h.f.hartman@student.utwente.nl
†Thales Nederland B.V., Hengelo, Netherlands

***Abstract*—Safely measuring high power conducted electromagnetic interference (EMI) is an issue to be addressed, where a possible measurement strategy is being discussed in this paper which uses the benefits of multi-channel synchronous time-domain electromagnetic interference (TDEMI) measurements. Only the differential mode (DM) voltage has been evaluated in this paper, however the setup is not limited in this respect. Common mode (CM) voltage can also be synchronously analyzed with this setup. Nevertheless, with respect to the to be measured amplitudes, DM voltages in this particular system offer a larger challenge and are addressed. The setup was developed with respect to Low-Frequency conducted EMI measurements in high power, fast switching systems using a low-cost solution.**

I. Introduction

As a result of the emerging new technologies and the rapid development of new electronic products, the ability to achieve electromagnetic compatibility and to improve it becomes a major challenge in the development of newer electronic products. Equipment to quickly and fully characterize a system's electromagnetic compatibility will result in a decrease of the costs of the system and it will also improve the quality in circuit and system development. Traditionally radio noise and electromagnetic interference were measured and characterized using superheterodyne radio receivers, which require measurement bandwidths, step sizes and dwell time. As has been shown in [1], this can result in extreme measurement times. The proposed solution is time-domain measurements in combination with digital signal processing (DSP).

Several time-domain electromagnetic interference (TDEMI) measurements have been studied extensively in for instance [2]–[4], with an increasing interest in the (fast) transient analysis [5], [6]. With [2] proposing to decompose the electromagnetic interference (EMI) in differential mode (DM) and common mode (CM), [5] decomposing the EMI transient phenomena in time domain through DSP, and [3], [6] to use short term fast Fourier transform (STFFT) techniques to present time-frequency plots (i.e. spectrograms). The TDEMI approach, as an alternative for EMI receiver, benefits [1], [4] and challenges [7], [8] have been addressed.

In this paper, the TDEMI approach is used for determining conducted interference originating from a Galium-Nitride (GaN) based DC/AC converter. As today's commercial of the shelf (COTS) power electronics have switching frequencies within the range of 2 kHz-150 kHz, for which civil emission standards are lacking [9], the low frequency (DC-30 MHz) conducted EMI frequency band is of great interest. This paper will focus on the evaluation of multichannel synchronous measurements as stated in [4] and the possible challenges it brings. Fig. 1 shows a quick overview of the measured parameters and used method.

xxx-x-xxxx-xxxx-x/xx/$31.00 © 2018 IEEE

An 8-channel scope is used in conjunction with the 'mains monitor box' as described in [9] and will be elaborated on in Section II. The goal is to compare different methods of measuring and calculating, via DSP, the DM voltage. Three separate methods are used to investigate the DM EMI:

- Symmetric Voltage Measurement (V_{dm})
- ΔNon-Symmetric Voltage Measurement ($V_L - V_N$)
- ΔNon-Symmetric Current Measurement ($I_L - I_N$)

Voltage and current measurements have an overlapping bandwidth from approximately 2 kHz to 100 kHz.

In the following section the measurement setup is briefly discussed, which is then followed by a discussion on the beneficial effect of multi-channel measurements. The results presented in section IV are qualitatively reviewed, as this is a proof-of-concept type of setup.

II. Measurement Setup

Safely measuring DM EMI in a relatively high voltage (i.e. above 100 V) setup is done as depicted in Fig. 2a. The inside of a conducted measurement device, as seen in Fig. 2a, can be seen in Fig. 2b and Fig. 2c. As the emphasis of this paper lies in synchronous time domain measurements, the functional behavior of the AC/DC converter will only be briefly described here.

A. GaN Half-bridge

In Fig. 2a it can be seen that the 'DC' source is a galvanic isolated grid that has been rectified. By using sinusoidal pulse width modulation (sPWM) driver logic, the switches are operated in such a way, that the switching node is either connected to the +165 V or -165 V. This results in a sPWM voltage waveform that contains two main frequency components, f_c and f_m, which are the switching frequency and AC output frequency respectively. [10], [11] describe the full background for studying a DC/AC converter with extreme flexibility in choosing these frequencies. However, in the evaluated setup

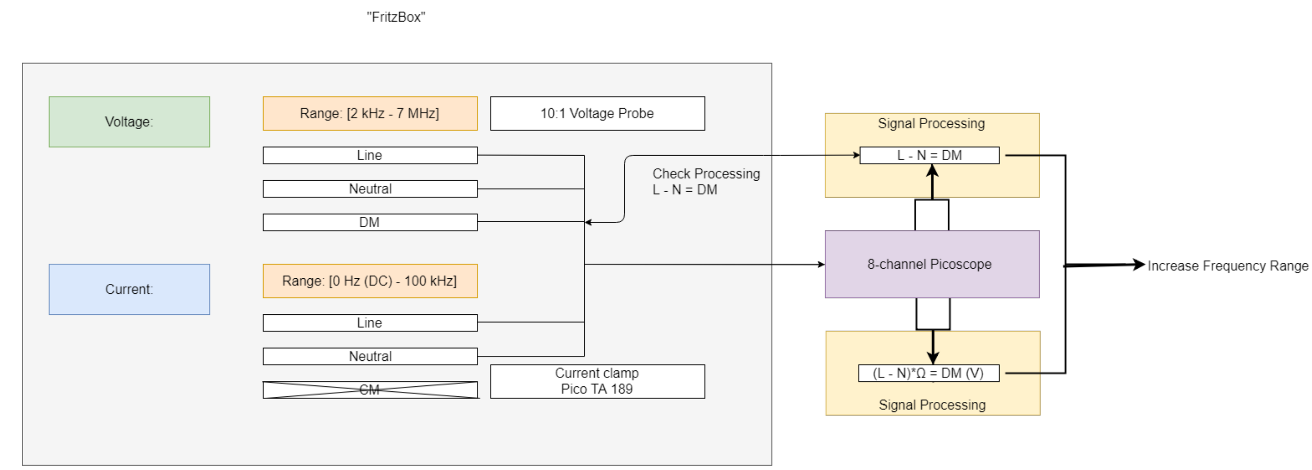

Fig. 1: General Overview

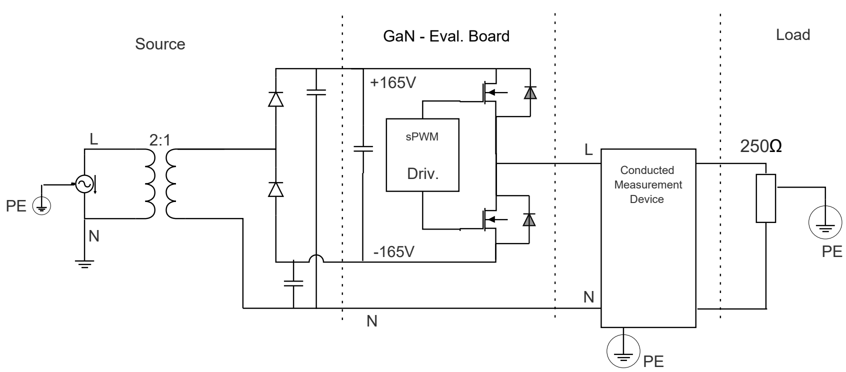

(a) setup

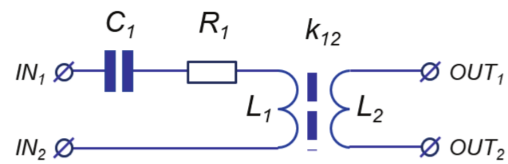

(b) Filter insulator implementation adopted from [9]

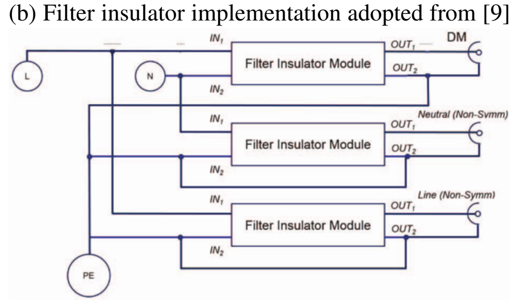

(c) A single phase implementation adopted from [9]

Fig. 2: Schematic representation of the conducted emission test setup

$f_c = 25\,\text{kHz}$ and $f_m = 50\,\text{Hz}$, which implies that, when the output waveform is low pass filtered, the resulting AC signal consists only of a 50 Hz component with an approximate $V_{rms} = 116\,\text{V}$.

B. Five channels

As the setup is evaluated for the use in operational high power switching electronics, three methods for determining the DM EMI were applied, which require the synchronous measurement of five separate parameters:

- V_{dm}: Differential mode Voltage
- V_L: Line Voltage
- V_N: Neutral Voltage
- I_L: Line Current
- I_N: Neutral Current

The used low-cost PicoScope functioning as an oscilloscope, has a maximum input voltage range of $\pm 50\,\text{V}$ and the possibility of measuring 8 channels at the same time. Table I summarizes the measurement equipment specifications. By combining the results from the current and voltage measurements, one is able to determine the conducted EMI from DC to 7 MHz without endangerment of the used scope. In the following section possible beneficial effects of DSP are discussed, while in section IV the acquired DM voltages are verified with an analog separated DM voltage.

III. Beneficial Effects of Multi-Channel Synchronous Conducted TDEMI Measurements

The previous section has described a type of switch mode power supply (SMPS) that is high power and has an operating frequency within the problematic low frequency conducted

TABLE I: Measurement Equipment

	Pico TA 189	"Meas. Box"
Quantity:	Current	Voltage
Measured Modes:	Line and Neutral	Line, Neutral and DM
Frequency Range:	DC - 100 kHz	2kHz - 7 MHz
Ratio's	1:10	1:50

EMI band. This section addresses possible benefits from using a multi-channel measurement setup.

A. Mode separation

Multi-channel measurements have shown the possibility to separate CM and DM (noise) signals through DSP, by measuring the line and neutral voltages in the time domain or the line and the neutral currents. In the measurement setup it was mentioned that only the DM voltage is studied.

As shown in [3] the symmetric DM Voltage can be calculated via the line and neutral voltage as follows:

$$V_{dm} = V_L - V_N$$

and indirectly via the line and neutral current as:

$$V_{dm} = (I_L - I_N) \cdot Z$$

Where in this case $Z = 250\,\Omega$ and is assumed to be constant over the entire frequency range.

B. Extended Frequency Range

By using the measurement box from [9], which is depicted in Fig. 2, the voltage measurement bandwidth ranges from 2 kHz until 7 MHz. This together with having a current meter going from DC to 100 kHz gives rise to the possibility to increase the total (one-shot measured) frequency range with respect to a single channel measurement, while maintaining a low noise floor. In [7] it is already discussed that there are challenges when using a single A/D converter (i.e. channel) with respect to the required dynamic range. As a verification, all three methods are displayed in Fig. 7. The frequency range displayed is the overlapping range of 2 kHz to 100 kHz.

As the results are from a 0.2 seconds measurement with a sampling rate of 40MHz, the possibilities for applying DSP are endless. In the following section the results will be presented without applying any DSP, apart from the one mentioned in this section. The results are presented following the overview given in Fig. 1.

IV. Results

At first the results are shown over the entire frequency range, 0 - 20 MHz. The different measurement techniques are plotted together on a logarithmic scale which can be seen in Fig. 3. Note that the signals are even plotted for frequencies outside the frequency ranges mentioned in Table I.

The next first logical step is then to only plot the respective frequency ranges of the different parts of the measurement set-up, which can be seen in Fig. 4

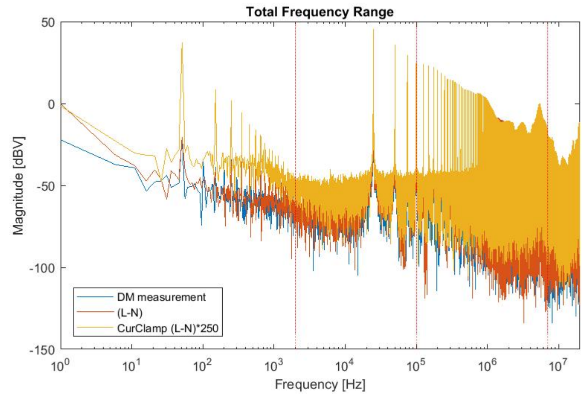

Fig. 3: Full Frequency Range

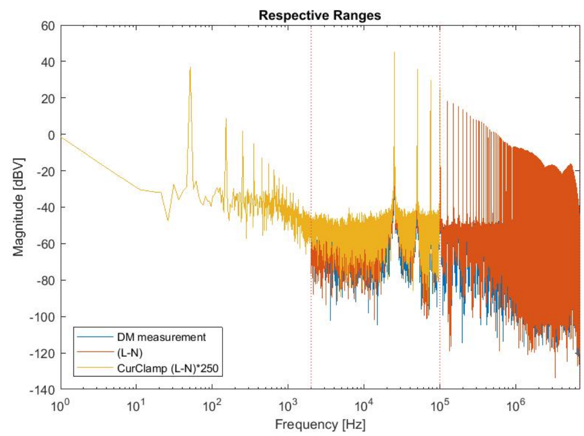

Fig. 4: Overlapping Respective Frequency Ranges

A. Separation results

Next the DM voltage measured directly and via DSP, by subtracting the neutral voltage from the line voltage, are compared. Such a comparison for their respective ranges is plotted in Fig. 5. To make a quantitative comparison the average difference in dB is calculated and found to be 0.3168 dB. Note that in the case of the analog separation one measures a single voltage, while in the digital separation, two signals are measured, which has an influence on the difference in noise levels. The assumption of the 1:50 ratio in the measurement setup, mentioned in Table I and elaborated on in [9] is related to component values used, which are assumed to be $2.5\,\mathrm{k}\Omega$ and $50\,\Omega$. However, as with any mass produced component, they are subjected to production errors. In case of the digital separation the ratio should be equal for line and neutral voltages. If not, a larger error can be introduced here than in the case of the analog separation. The average deviation of 0.3168 dB might have originated from this introduced error.

B. Comparison of methods

It is easily seen from the values in Table I that there is an overlapping range for the different measurement techniques between 2 kHz and 100 kHz. As a validation of extending

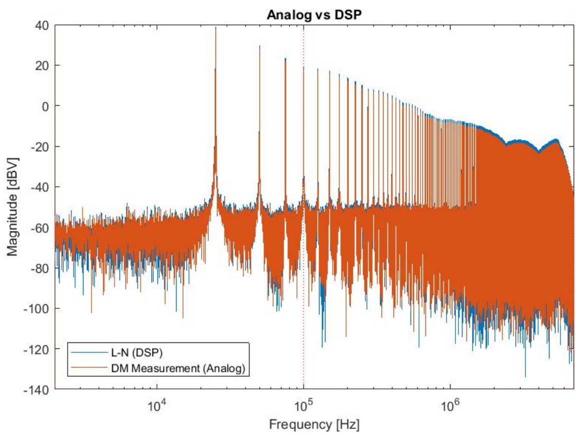

Fig. 5: Analog vs DSP

the frequency range by combining the separate measurement techniques, the found values within this range should be conform. The overlapping frequency range is plotted in Fig. 7. It can be quickly seen that the peaks are similar while using different measurement techniques. When looking at the average deviation between the signals it is found however that the calculated DM voltage via the current clamp deviates around 8 dB. This deviation is due to the higher noise floor which is apparent in the picture. However inspection of the first peak values (at 25kHz) for I_{L-N}, V_{DM} and V_{L-N} give 39dB, 37dB and 32dB respectively. As explained earlier, the large deviation of V_{L-N} might have originated from deviating component values. Comparing I_{L-N} and V_{DM}, shows a deviation of 2dB, which is relatively large. In case of the current measurement, a load of $250\,\Omega$ was assumed to be broadband.

Based on the above stated deviations, the voltage port transfer functions were measured to determine if the ratio is indeed 1:50. As is seen in Fig.6, there is a large deviation in the neutral port. After taking this into account, the peak values for V_{DM} and V_{L-N} are deviating by only 0.16dB.

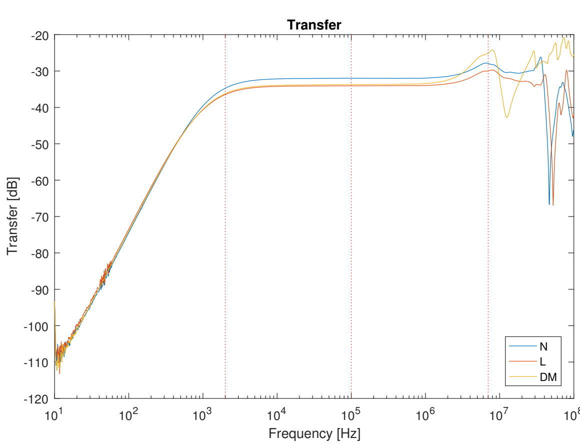

Fig. 6: Measured transfer functions of DM-, line and neutral voltage ports

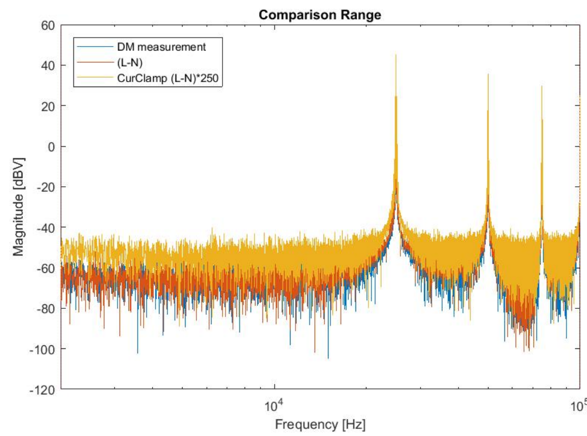

Fig. 7: Frequency Range Comparison

C. Extended Frequency Range

As the V_{DM} and V_{L-N} are deviating only slightly, the following graph, Fig. 8 is plotted using the voltage measurement results in the overlapping frequency range. This new extended frequency range is then plotted and can be seen in Fig. 9. Where the rough transition at the 2 kHz mark is due to the previously mentioned difference in noise levels and the falsely assumed load value.

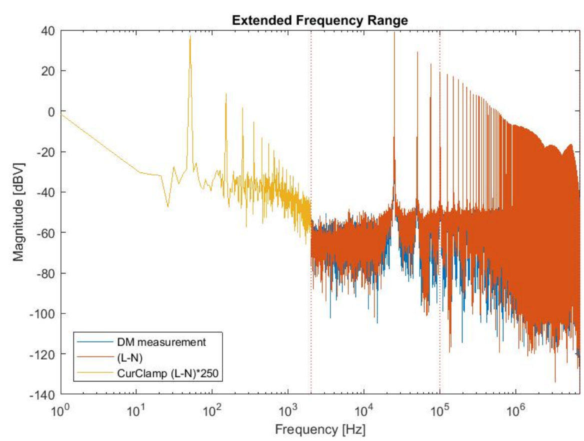

Fig. 8: Extended Frequency Range

V. Conclusion

With the aim to benefit from synchronous time domain measurements, an 8 channel measurement setup has been qualitatively evaluated. Possibilities for safely measuring high voltage applications have been discussed, with the enablement of noise mode separation. Mode separation through analog circuits as well as DSP have been discussed and found to have a negligible deviation. It has also been shown that by combining low-frequency current measurements with high-frequency voltage measurements, one can extend the frequency range of a single measurement, without compromising the signal to noise ratio due to the limited dynamic range of

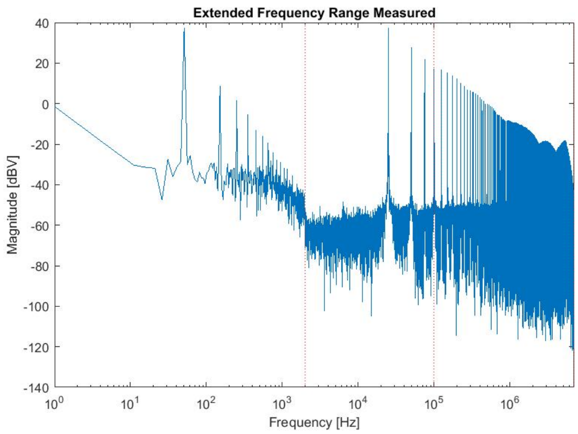

Fig. 9: 1 line Extended Frequency Range Measured DM voltage

an ADC. However in the measurement setup presented in this paper, the lack of a frequency dependent impedance measurement of the load resulted into a large deviation when comparing the overlapping frequency range. Nonetheless, it has been shown that it is possible to benefit from multi-channel synchronous conducted TDEMI measurements applied in high power electronic systems.

References

[1] I. Setiawan, N. Moonen, F. Buesink, and F. Leferink, "Efficient Magnetic Field Measurements," 2017.

[2] Y.-s. Lee, "Time Domain Measurement System for Conducted EMI and CM/DM Noise Signal Separation," *2005 International Conference on Power Electronics and Drives Systems*, vol. 2, pp. 1640–1645, 2005. [Online]. Available: http://ieeexplore.ieee.org/lpdocs/epic03/wrapper.htm?arnumber=1619951

[3] B. J. A. M. Van Leersum, R. B. Timens, F. J. K. Buesink, and F. B. J. Leferink, "Time domain methods for the analysis of conducted interference on the power supply network of complex installations," *IEEE International Symposium on Electromagnetic Compatibility*, pp. 605–610, 2014.

[4] M. Pous, M. Azpúrua, and F. Silva, "Benefits of Full Time-Domain EMI Measurements for Large Fixed Installation," pp. 514–519, 2016.

[5] M. A. Azpúrua, M. Pous, and F. Silva, "Decomposition of Electromagnetic Interferences in the Time-Domain," *IEEE Transactions on Electromagnetic Compatibility*, vol. 58, no. 2, pp. 385–392, 2016.

[6] I. Setiawan, C. Keyer, M. Azpurua, F. Silva, and F. Leferink, "Time-domain Measurement Technique to Analyze Cyclic Short-Time Interference in Power Supply Networks," pp. 279–282, 2016.

[7] E. Puri and M. Monti, "Hidden Aspects in CISPR 16-1-1 Full Compliant Fast Fourier Transform EMI Receivers," pp. 34–39, 2016.

[8] ——, "The Importance of Overload Revealing in EMI Receivers," 2017.

[9] C. Keyer, F. Buesink, and F. Leferink, "Mains Power Synchronous Conducted Noise Measurement in the 2 to 150 kHz band," pp. 865–869, 2016.

[10] N. Moonen, M. Gagic, F. Buesink, J. A. Ferreira, and F. Leferink, "Harmonic Cancellation in a Novel Multilevel Converter Topology for the Future Smart Grid," in *Electromagnetic Compatibility (EMC), Signal and Power Integrity (SIPI), 2017 IEEE International Symposium on*, Washington, 2017, p. to be published.

[11] N. Moonen, F. Buesink, and F. Leferink, "EMI Reduction in SPWM Driven SiC Converter Based on Carrier Frequency Selection," in *2017 International Symposium on Electromagnetic Compatibility - EMC EUROPE*, Angers, 2017, p. to be published.

RFI Estimation from Non-GSO Satellites Based on Two Line Element Assisted Equivalent Power Flux Density Calculations

Tom Hartman*, Niek Moonen*, Frank Leferink*†
*University of Twente, Enschede, Netherlands, t.h.f.hartman@student.utwente.nl
†Thales Nederland B.V., Hengelo, Netherlands

***Abstract*—As a result of out-of-band emissions and spurious emissions from air-borne or space-borne transmitters simulations and analysis methods have been developed. These methods were developed to determine the amount of interference such a transmitter could cause. The method discussed and applied in this paper is the equivalent power flux density (EPFD) method, which is formally described in international telecommunication union (ITU) recommendations. Up until this point this method has been implemented in MATLAB, which can be used for the determination of the amount of data loss in radio telescopes due to the unwanted emissions of the Iridium satellite constellation. In this paper, it is proposed to use the two line elements (TLEs) instead of the licensed Satellite ToolKit in the EPFD calculation. A theoretical case has been implemented, which is adaptable to the user preferences. The flexibility of the algorithm has been improved, while computational time remains in the same order of magnitude.**

I. Introduction

In radio astronomy, extremely sensitive radio antennas are used to detect very faint radio signals of cosmic origin. The strength of these signals are several orders of magnitude smaller than the radio signals used in for instance telecommunication services. Due to the radio frequency interference (RFI) susceptibility of the antennas, mitigation techniques need to be developed, for which RFI investigations are required [1]. The international telecommunication union (ITU) regulates the division of the radio spectrum and allocates frequency bands to different radio services. Some are dedicated solely to radio astronomy. This allocation means that radio astronomy can claim protection within these bands, however out-of-band emissions and spurious emissions may end up in these allocated bands and could then cause harmful interference [2]. To determine the RFI quantitatively, e.g. from the Iridium satellites, a simulation, measurements, and analysis methods have been developed [3]–[5]. For satellites in non-stationary orbits [6], such a method is the so-called equivalent power flux density (EPFD) method. This method calculates the detrimental influence of the several satellites in a certain constellation on a telescope. The power of this method lies in the fact that it takes the time invariant state of the system in consideration and creates an equivalent power flux density (PFD) evaluated at boresight.

In ECC Report 247 [5], the EPFD method and its implementation in MATLAB are described. In this paper, the downlink of the interference from non-geostationary orbiting (GSO) satellites onto radio telescopes is studied.

The challenges in the RFI determination are related to the non-stationary orbits. Gain and free space path loss (FSPL) are dependent on the relative position of an individual satellite, which is time varying. Info about satellite orbits are thus required for accurate estimation. Various solutions can be found for calculating or estimating orbits for individual satellites. The MATLAB implementation described in ECC Report 247 uses the Satellite ToolKit and is dependent on measurement data [5]. Keeping in mind that one requires a simplified perturbation model to estimate the state (i.e. position and velocity) of a satellite for any given time, the two line element (TLE) of the Iridium constellation was implemented. However, it is not limited to this particular constellation. Theoretically, it is required to consider the RFI contribution from all possible satellite constellations, taking into account their emitted electromagnetic interference (EMI) to create one overall EPFD evaluation.

Even with the use of the TLEs, the Python implementation still needed measurement data, e.g. from the Leeheim station, to make an analysis, which still kept the code restricted. For this reason, a theoretical case was implemented. This way, a quick theoretical calculation can be done to get a feeling of what impact a certain, possibly theoretical, constellation can have. This theoretical PFD can then make use of the positional data from the TLEs and makes it so that no stochastic approach is needed. This means that in this paper it is proposed to use the open-source format TLE to introduce flexibility in evaluating different satellite constellations and different radio telescopes, while using a deterministic PFD.

This paper starts with a theoretical background of the EPFD method, which is then followed up by a theoretical explanation of the stochastic process involved in the EPFD calculations. Then, the implementation is explained, where the focus lies on adding the TLEs. After this, the results are given followed up by a conclusion.

II. Theory: EPFD calculation

In case of GSO satellites, a simplified method for calculating the received power based on PFD is used, as the relative position of the satellite compared to the observer's position is constant. In case of non-GSO satellites, the relative position is varying, thus EPFD is proposed to incorporate the time invariant state of the system. This section derives an equation for calculating the EPFD. It originates from the overall power transfer function of a radio channel.

A. Power flux density

Friis transmission formula is seen in many different styles of writing. It simplifies radio link calculations to its basic components:

$$\frac{P_r}{P_e} = \frac{G_e G_r}{L_{fs}} = D_e D_r \Big(\frac{\lambda}{4\pi d}\Big)^2 = \frac{A_r A_e}{d^2 \lambda^2}$$

Where:

- $P_{e,r}$ - Power;
- $G_{e,r}$ - Gain;
- L_{fs} - Path loss;
- $D_{e,r}$ - Directivity;
- $A_{e,r}$ - Effective aperture area;

For RFI calculations, the same principle holds. In this case, the satellites are the emitting antennas, while the radio-telescope is considered to be the receiving antenna. Based on the assumption of ideal propagation, FSPL can be calculated from the distance between transmitter and receiver. The PFD is then defined as the amount of power per surface area that hits an observer that originated from an emitter at a certain distance, d:

$$\text{PFD} = \frac{P_e G_e}{4\pi d^2}$$

Note that the gain of the emitter includes directivity of the antenna and compensates for the assumption that transmitted power is distributed over a sphere with radius d, as if it were a isotropic radiator. The more commonly used form for PFD, in the analysis of EM radiation, is the flux of the Poynting vector. Combining the PFD and the assumed known effective aperture surface area (A_r) results in the received power. When considering a constellation of GSO satellites, the total PFD is a superposition of all contributing satellites:

$$\text{PFD} = \sum_{i=1}^{\#sat} \frac{P_{e,i} G_{e,i}}{4\pi d_i^2}$$

As mentioned, in case of GSO satellites this superposition of PFD method holds, as it can be assumed that P_{e_i},$G_{e,i}$ and d_i are constant and time invariant. In case of non-GSO satellites the relative positions are varying and requires a slightly different approach.

B. Equivalent Power Flux Density

EPFD calculation takes into account all emissions from non-GSO satellites at any given moment in time. At each unique time instance, the (directive) gain of the receiving antenna should be considered, i.e. the pointing of the receiver towards every source of interference. The methodology of EPFD considers the interference to be varying in time due to the varying relative positioning in space. Formally, EPFD is defined as [7] [8]:

$$\text{EPFD} = \sum_{i=1}^{\#sat} \frac{P_e G_{e,i}(\theta_i)}{4\pi d_i^2} \cdot \frac{G_{r,i}(\phi_i)}{G_{r_{max}}}$$

Time variant challenges that arise during the complex calculations:

1) P_e, time-variant and system dependent. However, in worst case scenario the maximum emitted power can be used.
2) θ_i, the off-axis angle between boresight of the emitter and the direction of the receiver.
3) $G_{e,i}(\theta_i)$, due to the rotation of the satellite this gain can vary over time.
4) ϕ_i, the off-axis angle between the pointing direction of the receiver and the direction of the emitter.
5) $G_{r,i}(\phi_i)$, the radiation pattern of the receiver is assumed to be known or estimated, therefore simplifying the calculation to only be dependent on the relative position of the interference source.
6) d_i, dependent on time, however can directly be calculated from the relative position of the transmitter.

Combining the power and gain of the noise source into an effective isotropic radiated power (EIRP) will result in the following equation:

$$\text{EPFD} = \sum_{i=1}^{\#sat} \frac{\text{EIRP}_i}{4\pi d_i^2} \cdot \frac{G_{r,i}(\phi_i)}{G_{r_{max}}} \tag{1}$$

Now that the calculation of EPFD is explained, its evaluation needs to be addressed. The goal of the RFI estimation is to determine the impact on astronomical measurements. In the next section it is explained how the ITU has made it possible to asses its impact.

III. Theory: Stochastic EPFD Evaluation

To determine the detrimental effects the emitted noise has on the astronomical data, a standard has been developed to display the results from the calculation shown in section II. It is based on the probability the constellation of satellites has on data-loss of astronomical data per part of the sky. A division is made, which is explained in the following subsection. After this, the computation stress of the stochastic analysis is discussed.

A. Sky-division Cells

To make a statistically valid EPFD, every possible point in the sky should be considered. For this reason, the sky is divided into rings and cells, defined in the ITU recommendation [7], [8]. The sky is described as 30 rings stacked on top of each other creating a dome, where each ring has a certain number of cells. The lower rings have the maximum number of cells, and the top rings have the least number of cells. This is because the top of the dome is smaller than the lower part. In a later subsection, it is explained how the code goes through all these rings and cells and how it chooses a random position within such a cell. Fig. 1 provides an example of the sky division found in Recommendation ITU-R M.1583-1 [7].

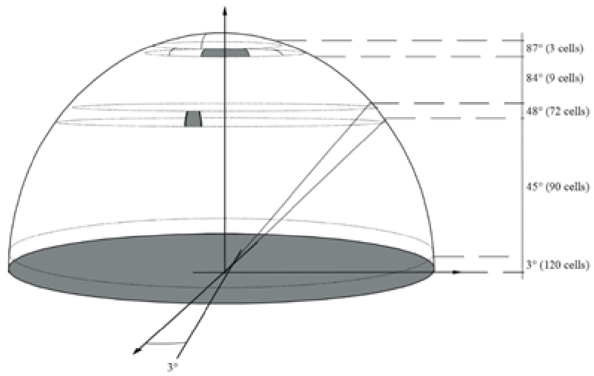

Fig. 1: Example of the Sky Division acoording to ITU-R M.1583-1

B. Computational Stress

In ITU-R M.1583-1, it is stated: "The methodology involves a number of trials, each of which calculates the averaged EPFD level over a 2000 s integration interval. A sufficient number of trials is needed to achieve the required confidence level in the results. In particular, the number of trials multiplied by the 2000 s integration time should be significantly higher than the period of the constellation" This results in parameter sweeps that need to be performed:

- Pointing of the Telescope, the direction in which the telescope is pointing within a certain cell.
- Moment in Orbit-Period, a time moment chosen within one orbit-period.
- Sky-division Cell, a cell chosen within the sky-division.
- Number of Satellites

With the Pointing and Moment parameters being random. The idea is to calculate the EPFD for different constellation moments, while considering a random pointing of the telescope within each cell. The goal is to obtain a statistical distribution of the EPFD in each considered cell. This is comparable to a Monte-Carlo type of simulation.

C. Data Loss Threshold

For every cell in the entire dome, the EPFD value is compared to the threshold found in [8]. The total number of times the threshold is exceeded is then added up and divided by the total number of cells. This is then defined as the data loss for one specific trial. This calculation is done over several trials, chosen to be five following the recommendations, from which a standard deviation and an average percentage are calculated. At this point, the power reduction needed to meet the 2% data loss threshold given by the ITU Recommendations [8] can be found. This is done by systematically lowering the total EPFD with steps of 1 dB, according to the recommendations. For every step, within the given range, a new average percentage is calculated. All these new average percentages are then plotted against their corresponding power increments. The amount, in dB, by which the EPFD needs to be reduced to get below the threshold, is then printed. Such a figure of the data losses can be seen in Fig. 2, where the actual reduction is found by taking the attenuation value found when the 2% value is passed.

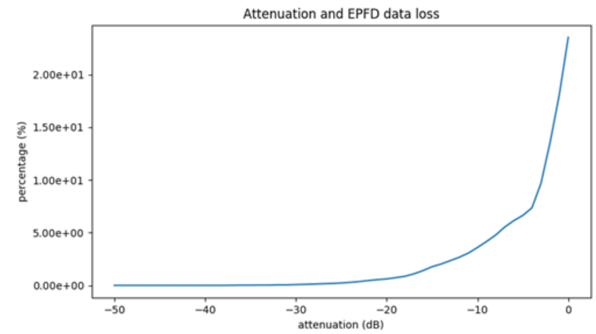

Fig. 2: The EPFD data loss for different EPFD value shifts

In the following section, the implementation of EPFD calculation is explained as it was recommended by the ITU. It focuses on the novelty that was added using TLEs and how it can be used as a solution to the time variant challenges as described previously.

IV. Implementation: Adding TLE

As the previous section has shown, calculating RFI from non-GSO satellites and its impact on radio astronomical measurements is a complex and elaborate endeavour. Therefore, in this section, equation (1) is used to simplify the RFI estimation.

In equation (1), the three main components of EPFD calculation can be distinguished:

- EIRP
- FSPL
- Weight

with:

$$\mathrm{PFD}_i = \frac{\mathrm{EIRP}_i}{4\pi d_i^2} = \frac{\mathrm{EIRP}_i}{\mathrm{FSPL}_i} \tag{2}$$

$$W_i = \frac{G_{r,i}(\phi_i)}{G_{r_{max}}} \tag{3}$$

To verify the correct implementation of equation (1), the MATLAB and Python implementation are compared through a qualitative analysis of the results. The results are obtained by using the same input data in both implementations. This is emphasized, since the novelty of using TLEs lies not in the implementation in Python, but in the more general way of determining the FSPL, as seen in equation (2), and the weight, defined as equation (3).

By using the proposed TLE method: EIRP_i is assumed (isotropic radiator) for simplicity, while W_i and d_i are derived from perturbation models that predict orbits of satellites. In the following subsections it is first explained how TLE support is added, followed by a solution for determining the elevation of a satellite.

A general overview of the changes implemented by using TLE's and the effects can be seen in Fig. 3.

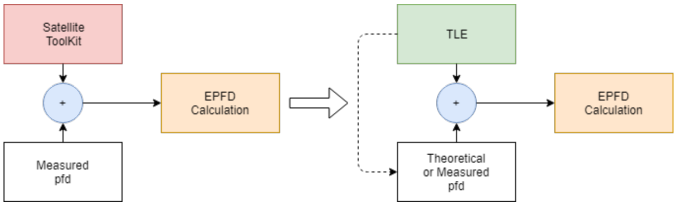

Fig. 3: New inputs for EPFD Calculations

A. Two line elements

Instead of making use of the Satellite ToolKit, TLEs were chosen to give the satellite constellations. TLEs are free to use and easily accessible on the internet. The info about which TLEs file to read is hardcoded into the program because only Iridium satellites were considered up until this point. This can be easily changed into an input for the user, but for now it is kept automatic. TLEs have a specific format for all satellites. It consists of three lines per satellite starting with a line which specifies the name and possibly the number of the satellite. This is then followed up by two lines including all the satellite information in a cryptic way. Within these two lines, the information about the satellite number, epoch date, and derivatives of the mean motion can be found, which can be easily read out. Frequently updated TLEs can be downloaded from sites like Celestrak [9], where it is just downloaded as a text file.

Using the sgp4 packet in Python, these two lines from the TLE can be read out. When doing so, several satellite objects are created. From these objects, characteristics such as position and velocity can be found. The position of a certain satellite can be called in a single line which needs a date and time as input. The created python code calls upon this position in a loop going through 1440 steps and increments the minute value of the input every time. The 1440 minutes were chosen to represent one day. All the positions of all the satellites for a specific day can be found, where the specific date is specified by the day at which the TLE was uploaded. This can be changed easily to be given as user input, where a specific day is given. Once all these positions are gathered, only the data points within sight of the telescope should be considered.

B. Changing the reference frame

Since the positions given in the TLEs files are in a Cartesian coordinate system with the centre of earth as the origin, a change of the reference frame is needed. The satellite positions relative to the radio telescope allow for simple determination of their elevation and distance. As can be seen in Fig. 4, the used coordinate system transformation consists of two rotational operations and a translation.

By first applying the rotational matrix multiplication as shown in equation (4), the translational operation becomes an additive constant along the rotated Z-axis that is equal to the Earth's radius (approx. 6371 km).

$$\mathbf{p_{sat}}' = \mathbf{M} \cdot \mathbf{p_{sat}} \tag{4}$$

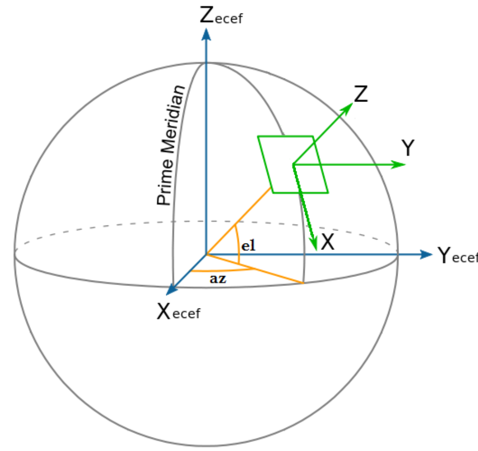

Fig. 4: Visualization of a change of the reference frame

In which the matrix $\mathbf{M}$ is defined as:

$$\mathbf{M} = \begin{bmatrix} \cos(az) & -\sin(az) & 0 \\ \sin(az) & \cos(az) & 0 \\ 0 & 0 & 1 \end{bmatrix} \cdot \begin{bmatrix} \sin(el) & 0 & \cos(el) \\ 0 & 1 & 0 \\ -\cos(el) & 0 & \sin(el) \end{bmatrix}$$

Where az and el are determined by the position of the arbitrary evaluated radio telescope and P_{sat} is the coordinate vector of a satellite, where the apostrophe denotes the new reference frame. In this specific case, it is assumed that the longitude and latitude coordinates are respectively the azimuth and elevation coordinates/angles.

By mere Cartesian to spherical coordinate transformation, the angle (ϕ_i) and distance (d_i) between the radio telescope and the satellite can be determined. If the elevation angle is positive, the satellite is in sight of the radio telescope. If the elevation is negative, the data point can be neglected, since it has no influence on the radio telescope.

To estimate the RFI and finally determine the impact a constellation of non-GSO satellites has on the astronomical data-loss, the EIRP should be determined.

C. Theoretical EIRP

Info about the power and the gain of the transmitter are required for calculating the EIRP per satellite. This data could be provided by measurements. However, due to lack of this data, a theoretical rule of thumb is used. The assumption made is a constant power multiplied by a gain of 1 W per 25 kHz. After this, an interference to carrier factor of -40 dB is used. Both of these values are based on related observations. Note that in this paper, it is irrelevant to use accurate values for the EIRP, as it a focuses on RFI estimations based on TLE assisted EPFD calculations. The novelty lies in incorporating the positional data of non-GSO satellites.

V. Results

A. Verification Results

Along the way of writing the new implementation, a lot of results were constantly checked with the existing MATLAB code. This was done because the MATLAB code was already approved and checked by the appropriate organizations. This

TABLE I: Verification Results

	MATLAB	Non-TLE Python
Frequency (MHz):	1610.6267	1610.6267
Integration time (s):	2000	2000
Data loss (%):	41.2082	40.9254
Statistical error (%):	0.88917	0.35268
Required reduction (dB):	18.3673	18

check was done one on one until the implementation of TLEs, where the results would deviate as expected due to the different input data and the newly implemented statistical approach. To check whether the actual EPFD method was implemented correctly, the data from the Satellite ToolKit used in the MATLAB code was used to do the calculations in Python once. If the result coincided within an expected statistical deviation, it could be concluded that the EPFD calculation was implemented correctly in Python according to the standards.

The results of such a comparison of MATLAB and Python using the Satellite ToolKit data can be seen in Table I. As can be seen in the table, only a small deviation between both data losses are found, which can be expected as a result of the statistical approach used for the EPFD calculation. The difference in the required reduction is due to the approach of how MATLAB goes through different value shifts.

B. Analyzing the evaluated EPFD

For each trial that the code is ran, the average data loss percentage over the entire sky for a specific frequency is calculated. The entire average data loss over the trials over the sky is plotted according to the way the sky is defined. Such a graph can be seen in Fig. 5, where the representation style is based on the figures created in the MATLAB code.

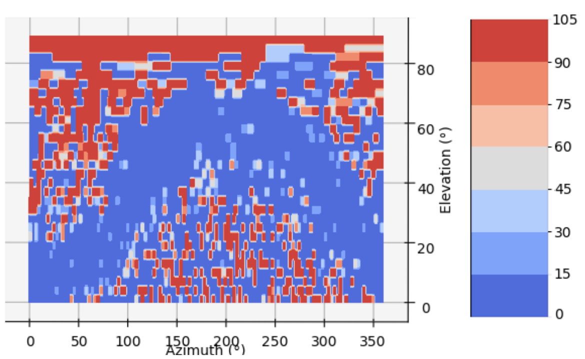

Fig. 5: Data loss over the sky

At this point, the reduction needed to get below the recommended threshold is calculated. It is plotted in Fig. 2 and all the results are then printed as can be seen in Fig. 6.

One could notice that different results are achieved when compared to the results shown in Table I. This difference arises from different input type files that have been used for the position of the satellites and a different position of the telescope. For the comparison, the Satellite ToolKit data was used, where the relative position to the telescope was already included. With the use of the TLEs the position of

```
Please give the filename of the data you wish to analyse:
30-04-2018

Percentage(s) with an integration time of 2000 s:
 [ 22.27934876  21.85089974  21.33676093  22.27934876  21.89374464]
Standard deviation with an integration time of 2000 s:
 0.347440187364
A reduction of 13 dB is needed to meet the requirements of a maximum loss of 2%
```

Fig. 6: General output of the Python code

the telescope has to be given as user input. For this run, an arbitrary Longitude an Latitude have been chosen resulting in a different data loss, which is not unexpected.

VI. Conclusion

It has been shown that the Python implementation gives the same results as the MATLAB implementation, considering the same input data. This was done to check whether the EPFD calculations were implemented correctly. Instead of the Satellite ToolKit the Python implementation makes use of TLEs, which are a lot more accessible, free to use, and are updated almost daily. Apart from the TLEs to make the code more accessible, a theoretical case has also been included. This theoretical addition is one specific case, but can be changed easily according to the circumstances the user expects. Via this, one can make an analysis of a certain, even entirely theoretical, constellation without having to have actual measurement data. These new additions make the Python code more accessible and usable for more separate cases.

It turned out that both the MATLAB and the Python implementation have similar computation times. Python, however, achieves this by using less data points. More data points are easily accessible with the Python code but this would hugely increase the computation time while only slightly increasing the accuracy.

Acknowledgment

This paper is based on an internship at Astron under supervision of dr. ir. Hans van der Marel.

References

[1] P. G. Wiid, H. C. Reader, and R. H. Geschke, "Radio frequency interference and lightning studies of a square Kilometre Array demonstrator structure," *IEEE Transactions on Electromagnetic Compatibility*, vol. 53, no. 2, pp. 543–547, 2011.

[2] S. Van De Beek, R. Vogt-Ardatjew, and F. Leferink, "Intentional electromagnetic interference through saturation of the RF front end," *2015 Asia-Pacific International Symposium on Electromagnetic Compatibility, APEMC 2015*, pp. 132–135, 2015.

[3] ECC, "ECC REPORT 171 IMPACT OF UNWANTED EMISSIONS OF IRIDIUM SATELLITES ON RADIOASTRONOMY OPERATIONS IN THE BAND 1610.6-1613.8 MHZ 0 EXECUTIVE SUMMARY," 2011.

[4] ——, "ECC REPORT 226 -Page 2 0 EXECUTIVE SUMMARY."

[5] ——, "Description of the software tool for processing of measurements data of IRIDIUM satellites at the Leeheim station," 2016.

[6] B. Levit and J. Lesh, "Radio Frequency Interference From Near-Earth Satellites," 1977.

[7] ITU, "Policy on Intellectual Property Right (IPR) Multichannel sound technology in home and broadcasting applications," pp. 2159–4, 2009.

[8] ——, "RECOMMENDATION ITU-R S . 1586 Calculation of unwanted emission levels produced by a non-geostationary fixed-satellite service system at radio astronomy sites ANNEX 1 Calculation of unwanted emission levels produced by a non-GSO FSS system at radio astrono," pp. 1586–1, 2002.

[9] NORAD, "CelesTrak: Current NORAD Two-Line Element Sets." [Online]. Available: https://www.celestrak.com/NORAD/elements/